University of Padua

Department of Physics and Astronomy "Galileo Galilei"

Master Degree in Astronomy

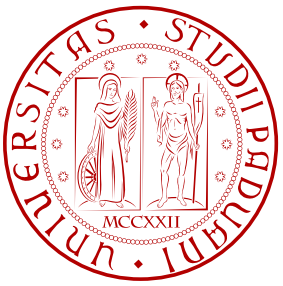

Search for Exoplanets in *K2* Open Clusters M 35 and NGC 2158

Supervisor: Prof. Giampaolo Piotto
Co-supervisors: Dr. Mattia Libralato
Dr. Domenico Nardiello

Student: Kaan Kaplan
Student ID: 1110256

ACADEMIC YEAR 2015-2016

Dedicated to
beloved brother
and father.
Rest in peace...

Contents

Chapter 1

EXOPLANETS AND DETECTION METHODS

In chapter one I start with the definition of the exoplanets, explaining how astronomers detect them. Then, we give a detailed description about the direct and indirect detection methods, how exoplanets can be found, which characteristics can be learned from these methods, how many exoplanets have been found so far.

In the 1963, the first exoplanet was announced in Nature Magazine. It was orbiting around Barnards star that is located 1.8 pc from the Earth. After almost ten years later this announcement was denied. People were witnessing the not genuine discoveries until the first exoplanet was discovered, in 1991. This detection was a milestone for exoplanet researchers. Researchers understood that these exoplanets were faint and too small with respect to their parent stars, making them hard to detect directly. Therefore, different methods were developed to find any signature of their presence around their host star. For example they were discovered thanks to the gravitational effects between host star and planet.

After decades, with the help of growing technology and improved instruments, scientist were able to find more and more exoplanet signals. Astronomers use some methods that can be direct and indirect. These different methods are sensible to only some characteristics of planets. The information gathered with these methods are complementary to each other and mandatory to completely shape the exoplanet system. With the help of the these different methods, researchers obtain a great deal of information about properties of planetary systems.

Up to now more than 4696 extrasolar planets have been found (http://exoplanetarchive.ipac.caltech.edu/). The detection techniques are grouped in direct and indirect methods.

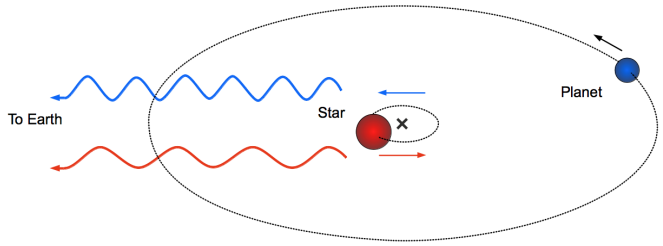

Figure 1.1: Example of blue/red-shift of the light coming from a star within an exoplanet orbiting around it. The doppler shift is due to the movement of the host star around the common center of mass of the system. (https://commons.wikimedia.org/wiki/File%3ARadial_Velocity_Exoplanet_Detection.png)

Direct method consists in the direct detection of the exoplanets from the image. However, it is very hard to achieve. Indirect methods refer to those methods that detect indirectly the presence of the planet: radial-velocity measurements, transit detections, astrometry, gravitational microlensing. Basically, radial-velocity measurements and transit method are good for detecting planets whose orbit is close to their parent star. Whereas, astrometry method is better for the detection of planets which have large orbital radius.

In the following sections I will describe these methods.

1.1 Indirect Methods

Astronomers had much better experience using indirect detection methods. They observe the effects on the host stars since planets and host stars orbit around the common center of mass.

1.1.1 Radial-Velocity Method

The radial-velocity method, also known as doppler shift, is one of the most successful planet finding method and many planets have been detected with it. The first exoplanet discovered with the radial-velocity method was discovered by Mayor and Queloz (1995). They analyzed the radial velocity signal obtained from the solar-type star 51 Peg, and found a Jupiter-mass planet orbiting around the star with a period of 4.23 d.

Basically, this method is based on analyzing the spectrum of the star. If a star hosts an exoplanet, it is possible to detect a change of its radial velocity

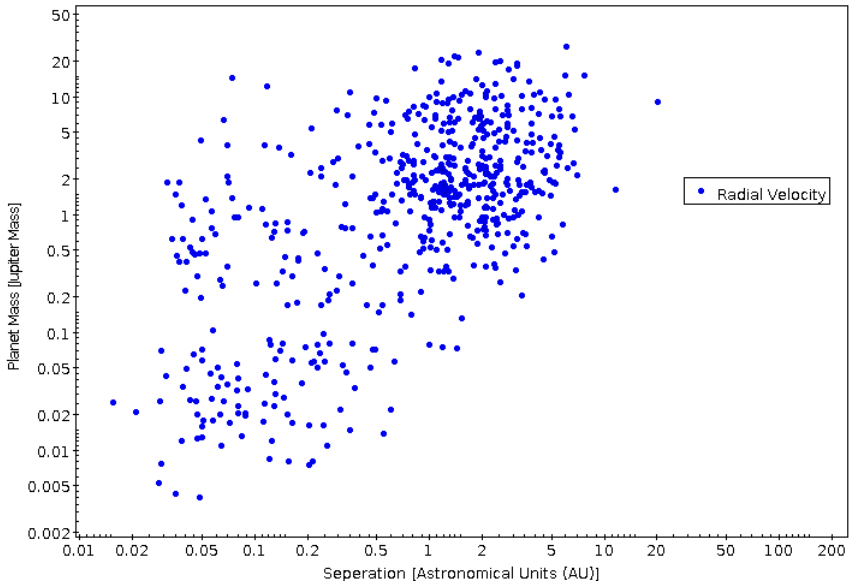

Figure 1.2: Planet mass as a function of the separation from their host star for planets discovered with radial-velocity method.
(Data from: http://exoplanetarchive.ipac.caltech.edu/)

due to its motion around the center of mass of the star-planet system. If the object is moving away from the observer, a red shift of the lines in the spectrum can be seen by the observer; if it is moving towards the observer a blue shift can instead be seen by the observer. In figure 1.1 an example of these blue/red are shown. The most important parameter that can be learned from the radial-velocity technique is the minimum mass $M_{\mathrm{P}} * sini$, M_{P} is the planet mass and i is the inclination of the planets orbit) of the planet.

For the future of the radial-velocity technique, the question is whether this method can be able to find smaller planets at large semi-major axis. Every year the number of detected exoplanet increases. However, to find the small size planet at wide orbital range, observers need more sensitive and precise instruments.

Up to now, 597 planets have been detected with radial-velocity method (http://exoplanetarchive.ipac.caltech.edu/). In figure 1.2 we plot the mass of the exoplanets discovered with the radial velocity method as a function of the separation from its host star (semi-major axis).

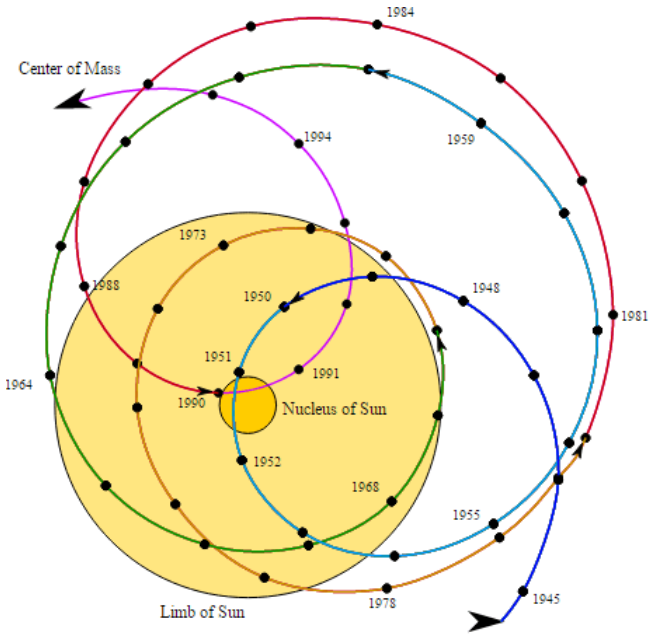

Figure 1.3: Planets and Sun are moving around the common center of mass. This figure is the representation of the changing of the center of mass during time.
(https://en.wikipedia.org/wiki/Methods_of_detecting_exoplanets)

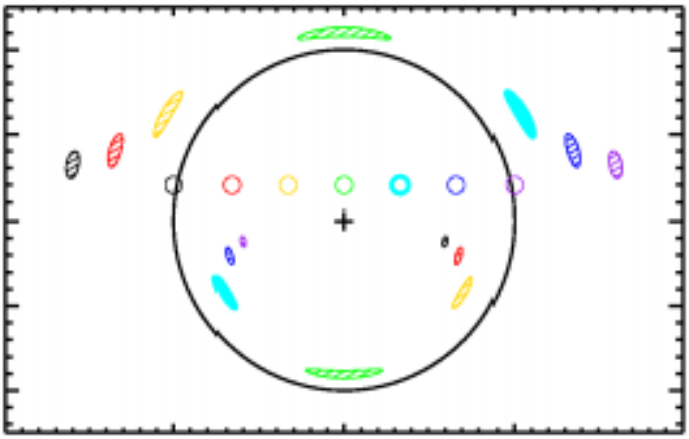

Figure 1.4: Background star is lensed by another foreground star, while the ellipses show the corresponding lensed image. Small circles displays the location of the source star. Largest black circle is the Einstein Ring. Plus symbol represents the lens star (Fischer et al. 2014).

1.1.2 Astrometric Method

Periodical changes in the position of the star can be caused by gravitational interaction between the star and its companion(s). In figure 1.3, the changing position of the Solar-system center of mass can be seen. Until now, the astrometric method has not been promising due to different limitations even if it is important because its results may be complementary with those coming from different techniques.

However, this method is hard to operate. Indeed, the astrometric signatures (wobble) of an exoplanet are very small and very hard to detect. Therefore it requires long temporal baselines and high astrometric precisions that are extremely hard to obtain with ground-based observations. So far, only one exoplanet has been detected with astrometric method (Sahlmann et al. 2013). Luckily, thanks to the accomplished launch of the Gaia satellite, searching of planets using astrometric method will be more promising than before.

1.1.3 Gravitational Microlensing

Gravitational microlensing stems from gravitational lens originally used for galaxies. An object (the lens) will bend the light that comes from background object (the source). This effect can produce various distorted and bright images of the source object. An excellent alignment of stellar objects will lead to symmetric images around the lensing object also called as Einstein

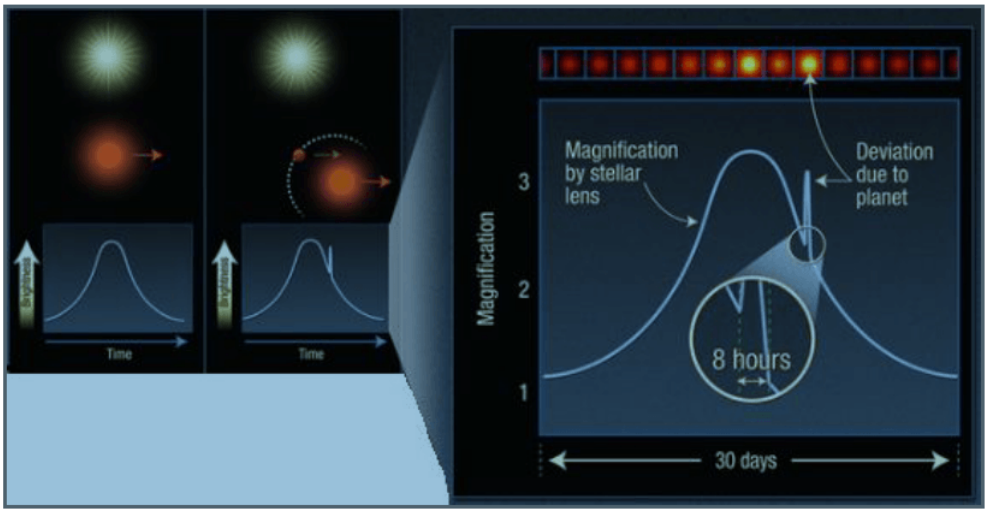

Figure 1.5: When the lens star (red) passes in front of background star, the brightness is increased (left). If there is a planet orbiting the lens star, it will create an additional spike.
(https://blogs.scientificamerican.com/life-unbounded/gravitational-mesolensing-and-the-hunt-for-exoplanet/))

ring (Renn et al. 1997). This event happens only if two objects are perfectly aligned. In figure 1.4 an example of the possible configuration is presented.

If two stars are perfectly aligned along the line of sight, a magnification of the lensed-star image can be observed. When the lensing star has a planet orbiting around, the gravitational effect of the planet makes an additional effect that it can be easily observed. The source star gets brighter, then there is a small spike of brightness due to the planet orbiting around the lens star. As soon as the lens star moves out of the alignment, the brightness of the background star starts to decrease (see figure 1.5).

Astronomers cannot foresee these lensing events. They can not predict where and when lensing events will occur. Therefore, they have to observe a wide area for long periods. The chance to observe two stars along the same line of sight is around one in 10^{-6} (Schneider et al. 1999). Due to the high number of stars in the Galactic bulge, the gravitational microlensing method could be an alternative method to find planets between Earth and center of the Galaxy.

The microlensing event is good for finding planets within few AU (Perryman et al. 2000) from Sun-like stars. However, with this method it is impossible to repeat a measurement because the chance of having two stars on the same line of sight twice is zero. The only parameters that can be learned

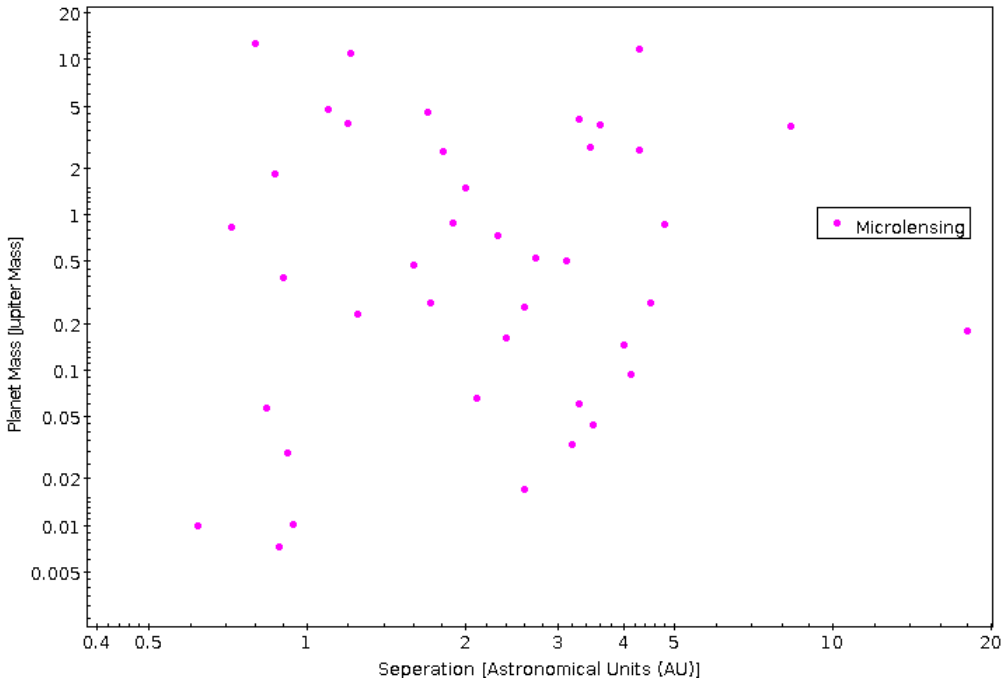

Figure 1.6: Same as figure 1.2 but for planets discovered by gravitational microlensing. (Data from: http://exoplanetarchive.ipac.caltech.edu/)

from the lensing event are the mass and orbital distance of the planet.

Sometimes exoplanets are not hosted by any star (the so-called free-floating planets) and the microlensing method is probably the only way to detect them. Furthermore, with accurate observations of the background stars, the microlensing method should show how often these microlensing events can be seen.

Up to now only 41 planets were discovered with this method (http://exoplanetarchive.ipac.caltech.edu/). In figure 1.6 green dots represent the planets found by gravitational microlensing method in the planet-mass versus seperation plane.

1.1.4 Transit Method

Up to now, all methods were aimed to detect the gravitational effects of the planet on stars. Transit method measures the fraction of star light blocked by a planet passing along the line of sight and give information about the size of the planet.

As soon as the exoplanet passes in front of the host star, it will cause a decrease of certain amount of star's light at every orbit. Exact measurement

of the star's brightness can display transit events.

The first exoplanet found by transit method was HD209458b. The planet was first discovered with the radial-velocity method then with a photometric follow-up a transit event was found. The transit depth due to HD209458b was about 1.7% of the star flux (Charbonneau et al. 2000 and Henry et al. 2000).

The major benefit of the transit method is that the size of the planet can be measured from the transits. Therefore, once the mass of the exoplanet is known from radial-velocity measurements, the density of the planet can be estimated, allowing astronomers to gather information about the physical properties of the exoplanets.

Major drawback of this method is that orbital plane of the planet should be across the line of sight of the observer. Another problem could be the presence of background eclipsing binaries that could mime a planetary transit in the light curves.

After 2009, the number of detected planets beyond the solar system with transit method increased thanks to NASA's *Kepler* mission. It was a milestone for the exoplanet detection until a reaction-wheel failure in 2013 (detailed information in Chapter 2).

Until now, 2693 exoplanets have been discovered by the transit method (http://exoplanetarchive.ipac.caltech.edu/). In figure 1.7 we plot mass versus semi-major axis for transiting exoplanets.

1.2 Direct Method: Direct Imaging

A tiny fraction of light coming from the exoplanet can sometimes be detected. However, in general it is very hard to find a possible exoplanet and hard to detect directly from its parent star.

Exoplanets can be detected with their thermal emission. If the host star is Sun-like star, and the planet is big (possibly bigger than Jupiter), it can be detected around its host star. If the planet is hot enough that emits thermal radiation, then in the infrared images possible exoplanets will be more brighter than at visible wavelengths. Furthermore, in the infrared regime the difference between star and planet emission is larger, and hence the planet is more detectable. The biggest challenge for astronomers is to separate the light that is coming from the possible exoplanet from its host star. This problem can be solved by using Point Spread Function (PSF) subtraction, coronagraphs and adaptive optics.

The idea consists in subtracting the unwanted light and highlight the other objects in the image. Coronagraphs are designed to prevent the light

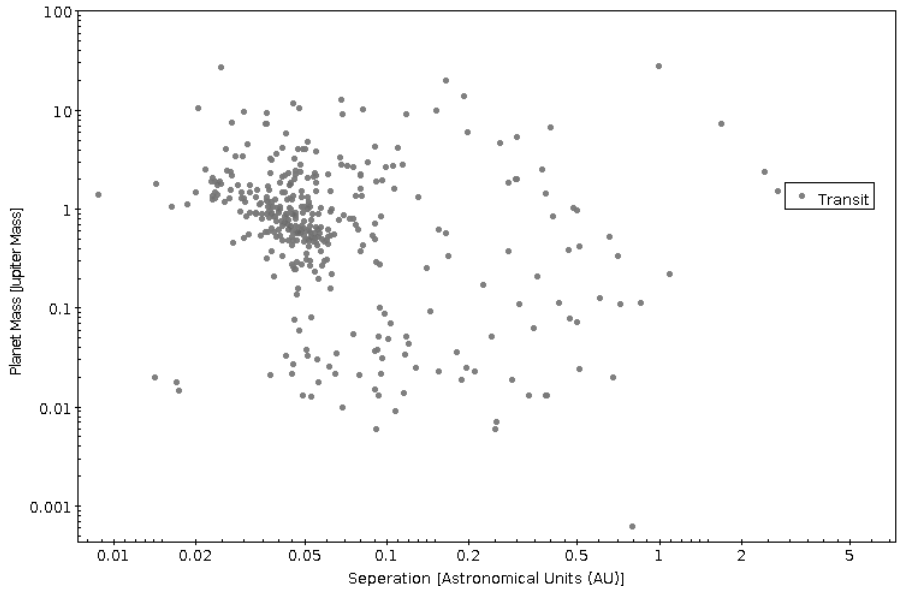

Figure 1.7: As in figures 1.2 and 1.6 but for planets detected by transit method. (Data from: http://exoplanetarchive.ipac.caltech.edu/)

coming from the star to reach the focal plane. Originally they were used to only study the corona of the sun. In figure 1.8 there is an example of chronographic image of star Fomalhaut and its planet Fomalhaut b taken with *HST* (*Hubble Space Telescope*) STIS (Space Telescope Imaging Spectrograph, Kalas et al. 2013). Coronagraphs are becoming main equipments for telescope that directly image exoplanets with ground-based facilities. Observations from the ground encounter the problem of the atmospheric turbulence. In figure 1.9, there is an example of the direct detection of HR8799 planets.

A promising instrument for exoplanet direct imaging is SPHERE (Spectro-Polarimetric High-contrast Exoplanet REsearch instrument) placed on VLT (Very Large Telescope) (Beuzit et al. 2008). SPHERE is a planet hunter that uses adaptive optics and a chronographic system and its aim is to find giant exoplanets orbiting stars.

Despite its promising results, direct imaging method for finding the planets beyond Solar System, is still i progress. Astronomers have high expectation that in the near future this method will be an important way to understand the characterization of exoplanets such as atmospheric compositions. With this method, only 43 planets have been discovered so far (http://exoplanetarchive.ipac.caltech.edu/).

In figure 1.10, there is an overview plot mass vs. separation in which all

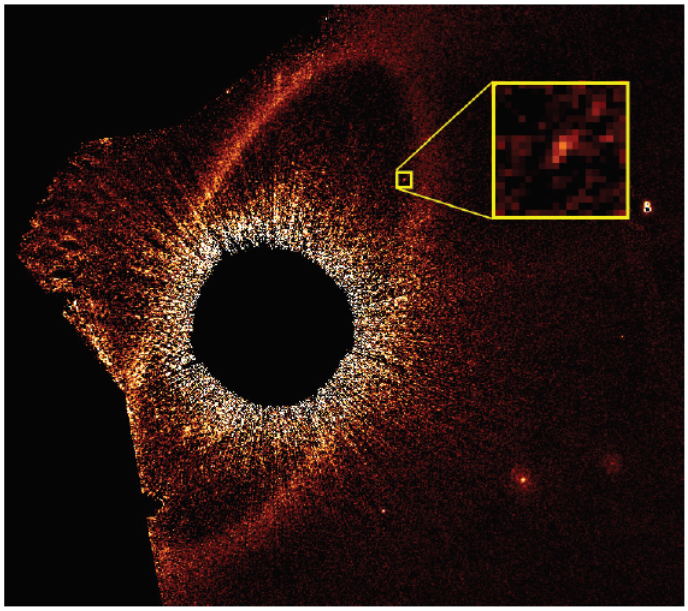

Figure 1.8: Chronagraphic image of Fomalhaut and Fomalhaut b. Coronograph blocks a large fraction of light from the host star and therefore the exoplanet in the small square can be detected (Kalas et al. 2013).

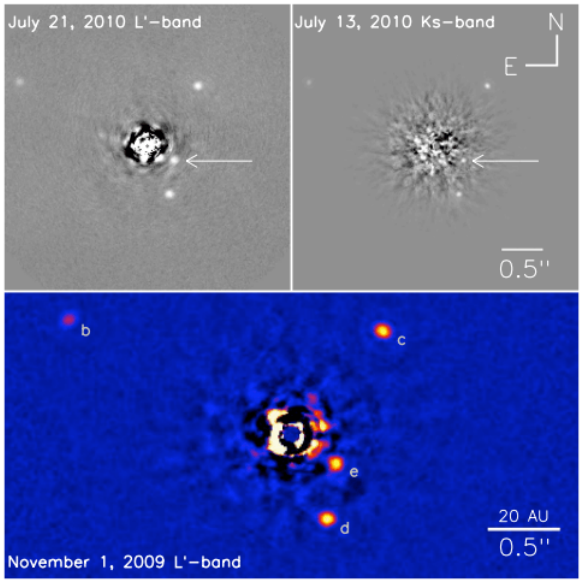

Figure 1.9: HR8799 observed with Gemini telescope in Hawaii, using adaptive optics to achieve observation in the infrared. Four planets are visible after PSF subtraction of the host star (Marois et al. 2010).

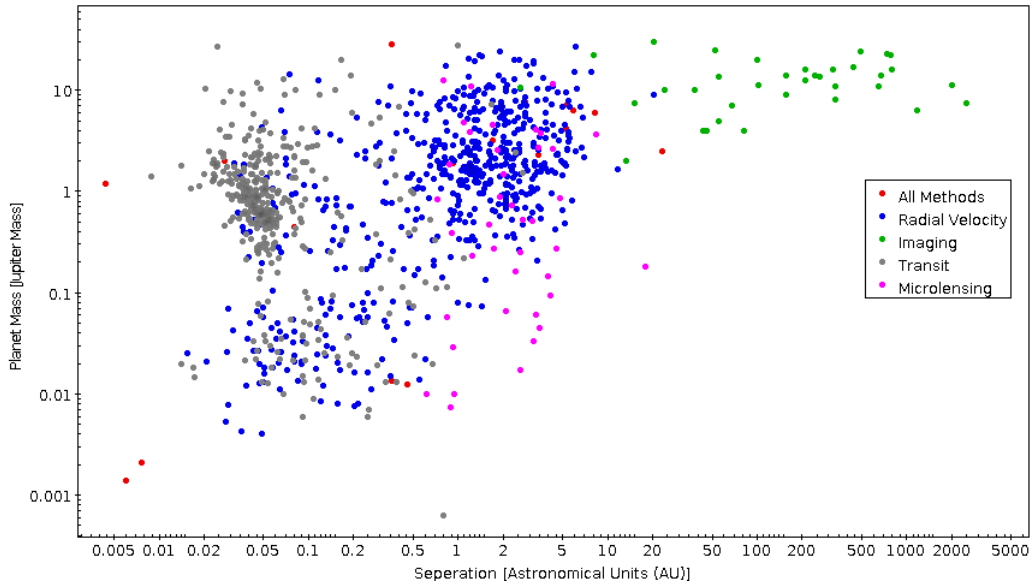

Figure 1.10: Mass vs. semi-major axis representation of all detection methods. Blue dots represent planets discovered with radial-velocity technique, red dots those with transits, black dots with direct imaging and orange dots with gravitational microlensing (Data from: http://exoplanetarchive.ipac.caltech.edu/)

methods described before are collected. It is clear that each method is more sensible to different kind of planets and planetary architectures.

Chapter 2

Kepler and *K2*

Chapter 2 gives a general description of the *Kepler* spacecraft, how this mission was started, what were the properties and the capabilities of the spacecraft. Detailed information about the *Kepler* mission and its aim are provided. Then how *K2* mission was born and what are the properties of this mission and capabilities with remaining two reaction wheels are presented.

2.1 *Kepler*

In 2009, *Kepler* was launched as an important National Aeronautics and Space Administration (NASA) mission, which main goal was to search planetary systems beyond solar system in order to catch transit events due to exoplanets orbiting around stars. An important purpose is to find Earth-size planets in the habitable zone of sun-like stars.

Almost all planets discovered before *Kepler* were giant planets, with a size as that of Jupiter or larger. *Kepler* was instead searching for Earth-like planets.

The *Kepler* mission made possible to find planets in a one-year orbit around Sun-like stars. The spacecraft observed a field with high-precision photometry in a 105-square-degrees area in the Cygnus and Lyra Constellations which has nearly 165,000 stars. The plan was to observe this region of the space for nearly 4 years imaging preselected objects. The obtained data from these areas was downloaded to ground as small images.

Kepler also provided data for asteroseismology, nearby main sequence stars with K_{P} magnitude down to 12. With the information gathered from these observations, astronomers could obtain characteristic data from so many stars even from red giants. This was the main purpose of the *Kepler* Asteroseismic Investigation (KAI) (Dalsgaard et al. 2010).

A major goal of the KAI was to characterize the host stars in planetary system using asteroseismology obtained from *Kepler*. Also, KAI made possible to analyze evolutionary state, age of the stars and stellar rotation. Therefore, the mission helped astronomers to understand the physics of the internal and external structure of the stars.

2.1.1 The Goal of the Mission

The scientific goals of the *Kepler* mission were described in several papers (e.g., Borucki et al. 2005, Koch et al. 2004, Koch et al. 2006) and can be summarized as follows:

- To analyse the frequency of planets inside and around the habitable zone of a lot of stars from different spectral types,
- To learn more about characteristics of candidate exoplanets,
- To determine the frequency and the orbital properties of exoplanets in multi-planetary systems,
- To understand the stars that are in the multi-planetary system.

The main purpose of the mission was to find exoplanets in the habitable zone around sun-like stars. For this range, nearly one year was needed to the exoplanet to complete the orbital period around host star. In order to find a reliable series, astronomers needed 4 transit events, which means almost 3 years required to detect a genuine exoplanet.

2.1.2 About the Spacecraft

Kepler contacted the ground two times in a week to upload the collected data, get essential command to continue the mission and update spacecraft status in order to understand whether it works properly or not. However, to be in the space and especially far away from Earth makes it impossible to fix any kind of breakdown.

2.1.3 Instrumentation

A 0.95-meter Schmidt telescope is operating on the *Kepler* Spacecraft, covering a wide field of view, nearly 105 square degrees. *Kepler* telescope is equipped with 42 CCDs and 4 fine guidance sensors located on the corners of the focal plane. Every CCD is made by two 1024×1024-pixel^2 channels

and the pixel scale is about 4 arcsec pixel^{-1} In figure 2.1 there is a picture of this focal plane. In 2010, there was a failure with module 3 and then in 2014 there was a second in in module 7. Therefore, right now 76 remaining channels are active. *Kepler* focused the same area during the whole mission and constantly followed up the brightness of nearly 100,000 stars for minimum 3.5 years.

2.1.4 Detection of Possible Candidates

When *Kepler* completed gathering data, it delivered it to the ground. Each small stamp of pixel in which a given star was imaged was processed to extract a light curve (using aperture photometry). Each raw light curve was corrected for systematic trends that could harm the transit detectability. When the best light curve was obtained, the light curve is searched for transit-like events. If a given light curve shows different flux drops that could be related to the presence of a planet, the object is promoted to *Kepler* Object of Interest (KOI). The KOIs are then further analyzed to understand if they are true, genuine candidates or spurious objects like blended eclipsing binaries in the background of the target that can mime transit events.

If a star has not been discarded yet, different follow-ups (e.g., high-contrast imaging) with other telescopes are performed. Objects that pass these processes are called *Kepler* exoplanet candidates.

The validation tests are not perfect, since peculiar objects like multiple-planet systems or circumbinary planets may show different features from the classical single-planet transits.

More than 4696 planet candidates have been detected so far from all missions, nearly 3396 of them have been confirmed and 2327 of them found by *Kepler* (http://exoplanetarchive.ipac.caltech.edu/).

2.1.5 Reaction Wheel Failure

On July 14, 2012 while *Kepler* was doing its main mission, it had encountered a reaction-wheel failure which was crucial for spacecraft to continue a proper attitude control. Basically, *Kepler* had 4 reaction wheels. They were used to slightly move and point the telescope, keeping the spacecraft stable.

Kepler only needed 3 reaction wheels to hold a stable pointing control of the telescope. However, another reaction-wheel failure made spacecraft unable to point its target field. NASA engineers focused on repairing two reaction wheels or at least one to keep stable the telescope. Unfortunately, they could not manage to restore them and stopped the *Kepler* main mission. Spacecraft was kept in the safe mode until a solution was found.

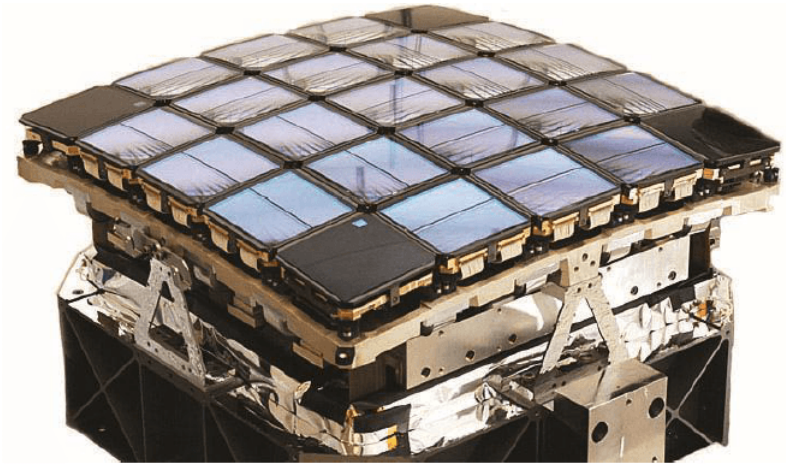

Figure 2.1: *Kepler* focal plane consists of 42 CCDs for high quality scientific observation.On the corners, 4 guiding sensors are present. (http://Kepler.nasa.gov/Mission/)

Then astronomers that contributed to the *Kepler* mission tried to find a way to operate the mission with remaining two reaction wheels. After different tests, *Kepler* team and NASA found a solution to continue to use *Kepler* and its telescope. This way the new *Kepler*-2.0, or simply *K2*, mission was able to continue its hunting with new feature and goals.

2.2 *K2*

More than two thousands transiting planets orbiting around their parent stars have been discovered by *Kepler* since 2009. Unfortunately, in 2013 *Kepler* mission ended because of the failure of two *Kepler*-spacecraft reaction wheels. For this reason *Kepler* was not able to keep the same accurate, stable pointing as during the main mission. NASA found a way to maintain the spacecraft stable using solar radiation pressure, the two still-working reaction wheels and the spacecraft thrusters, and therefore continue to collect data. This is how *K2* born (Howell et al. 2014).

The name *K2* could be chosen due to second *Kepler* mission or *Kepler* spacecraft with two reaction wheels. The main purpose of the *K2* is to observe close to the ecliptic plane, imaging various target fields. The new *K2* mission makes possible to observe new fields and gives opportunity to find important objects in previously-avoided areas of the Galaxy.

K2 is operated in three different axes using remaining two reaction wheels (Putnam & Weber, 2014). Figure 2.2 shows an outline of the three different

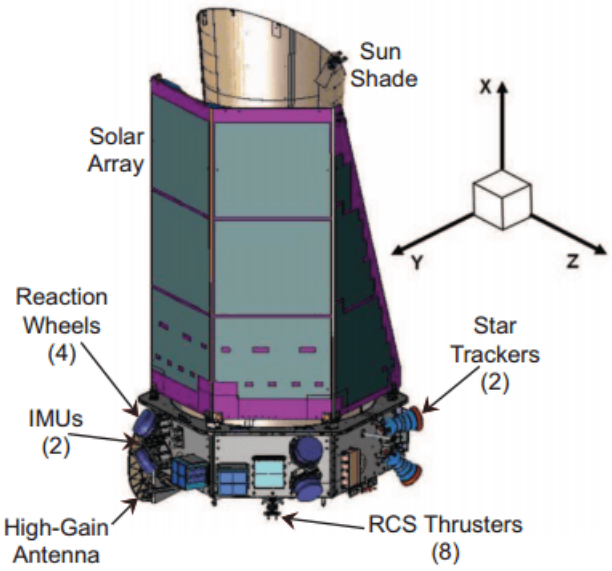

Figure 2.2: Representation of spacecraft coordinate system and its main components (Howell et al. 2014).

axes. *Kepler* team found a way to keep stable the spacecraft versus solar radiation pressure. By pointing spacecraft away from the sun, keeping the *Kepler*s orbit and equalizing the solar panels of the *Kepler* using solar pressure, they were able to produce a minimum disturbance along the X-axis (Howell et al. 2014). With precision and carefully choice of the roll angle and also rearranging the drift every 6 hours, the spacecraft can hold a steady and accurate pointing. Besides, the remaining two reaction wheels keep the spacecraft stable along Y and Z-axes.

K2 continues tracking and analyzing several field during the so-called *K2* campaigns. The duration of each campaign is constrained by the Sun light (figure 2.3) and it is restricted at about 75 days.

The total duration of one of the *K2* campaigns is about 83 days, 75 days of which are used to observe the target field and the remaining 8 days are dedicated to either to preparation for the selection of the next campaign or the downlink of the data. Figure 2.4 represents the outline of *K2* campaigns.

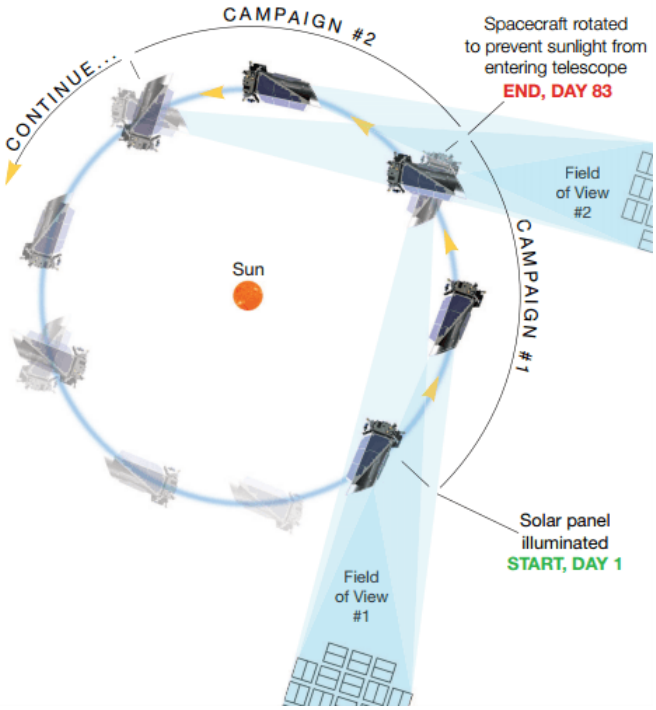

Figure 2.3: Example of *Kepler* spacecraft pointing during *K2* (Howell et al. 2014). Every about 83 days the *Kepler* spacecraft has to rotate in order to avoid Sun light entering in the telescope.

Up to now (2016, Oct 2), *K2* has completed observing 10 campaigns. According to NASA *K2* website there are 17 fields that have been or are planned to be observed and there will be even more of them in the future. Figure 2.5 shows the location of the old campaigns and possible future campaigns. During these 10 campaigns 11 open clusters (M 35, NGC 2158, M 45, NGC 1647, Hyades, M 44, M 67, NGC 6717, M 21, M 18, M 25), 3 globular clusters (M 4, M 80, M 19) and one nebula (M 8) has been observed. In this thesis, I focused my exoplanet search in the open clusters M 35 and NGC 2158 imaged during *K2* Campaign 0.

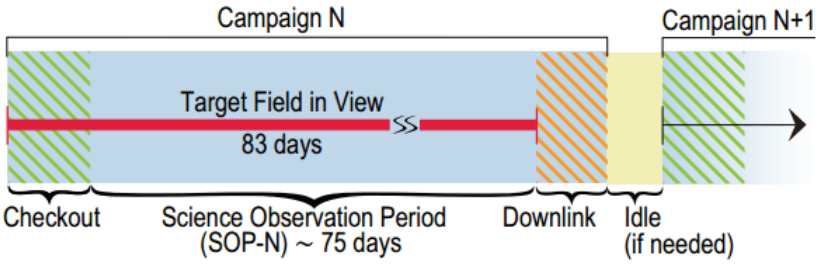

Figure 2.4: Example of *K2* campaign time line (Howell et al. 2014).

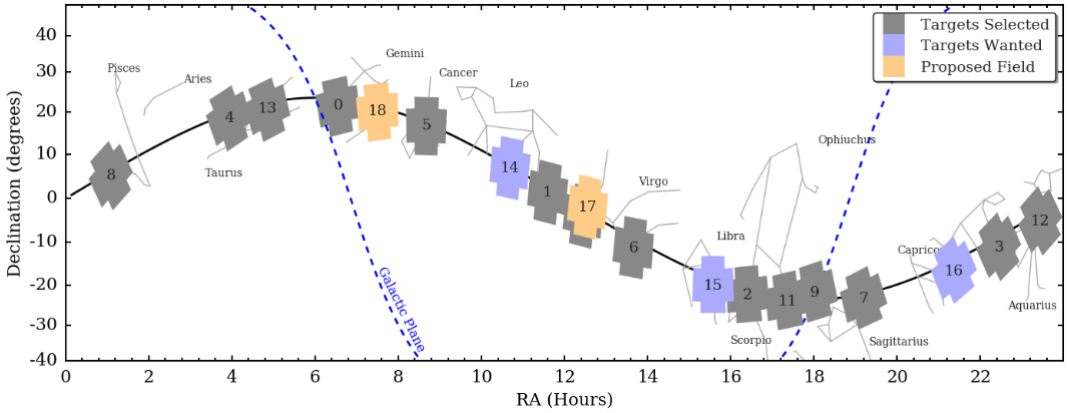

Figure 2.5: Overview of the already observed and planned *K2* campaigns. (http://Keplerscience.arc.nasa.gov/K2-fields.html)

Chapter 3

A PSF-BASED APPROACH TO *K2* DATA

In chapter three, I describe the method developed in Libralato et al. (2016a) to extract high-precision photometry for faint stars and in crowded environments from *K2* data. Hereafter, I will present the *K2* data at the basis of this thesis, and summarize the approach of Libralato et al. (2016a) for the light-curve extraction and systematic correction.

In most of *Kepler* and *K2* works, astronomers use aperture photometry. However, astronomers sometimes could not properly exploit their data with it. *Kepler*s undersampled images and stellar crowding make aperture photometry hard to use to get high photometric precision.

A new method, that makes use of Point Spread Function (PSF) and high-resolution catalogs, was presented by Libralato et al. (2016a). A key role is made by PSF neighbor subtraction (subtracting a stars neighbors before measuring its flux). By doing this, the light contamination effect during the analysis were decreased, allowing a better measure of faint objects in the area. Basically, there are four key ingredients for this process: image reconstruction, reliable PSF models, photometry and high-angular-resolution input list. Hereafter I will briefly discuss them.

3.1 Image Reconstruction

In this campaign, the authors focused on the open clusters M 35 and NGC 2158 and downloaded all target pixel files (TPFs) which have the data about time series. Figure 3.1 shows the pointing of *K2*/Campaign 0 (hereafter C0). Instead of working with small, individual pixel stamps as those in the TPFs, the authors reconstructed a full-frame image for each instant of the time se-

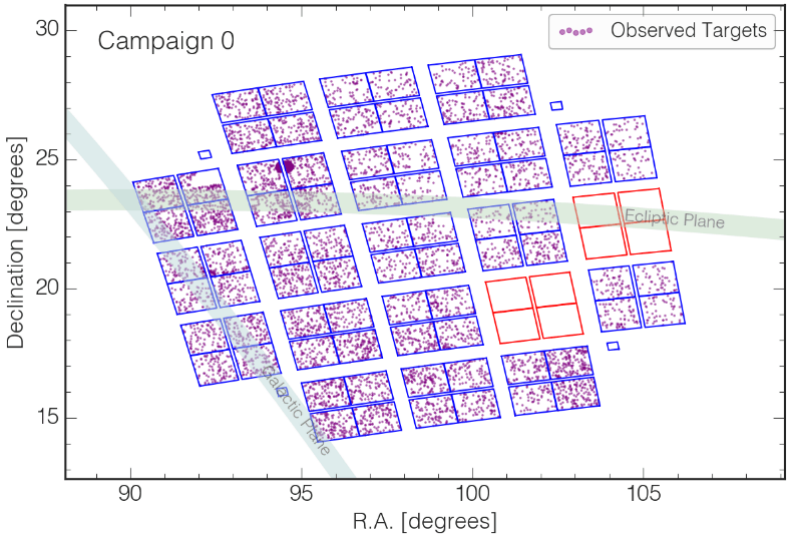

Figure 3.1: Schematic representation of *K2*/C0 field of view.
(https://keplerscience.arc.nasa.gov/images/campaign_selected/C0_selected.png)

ries of the TPF. This choice allowed the authors to better understand and analyse the characteristic of the images. Furthermore, they constructed only images for channel 81. 2422 images has beed used. In figure 3.2 these image and channel can be seen.

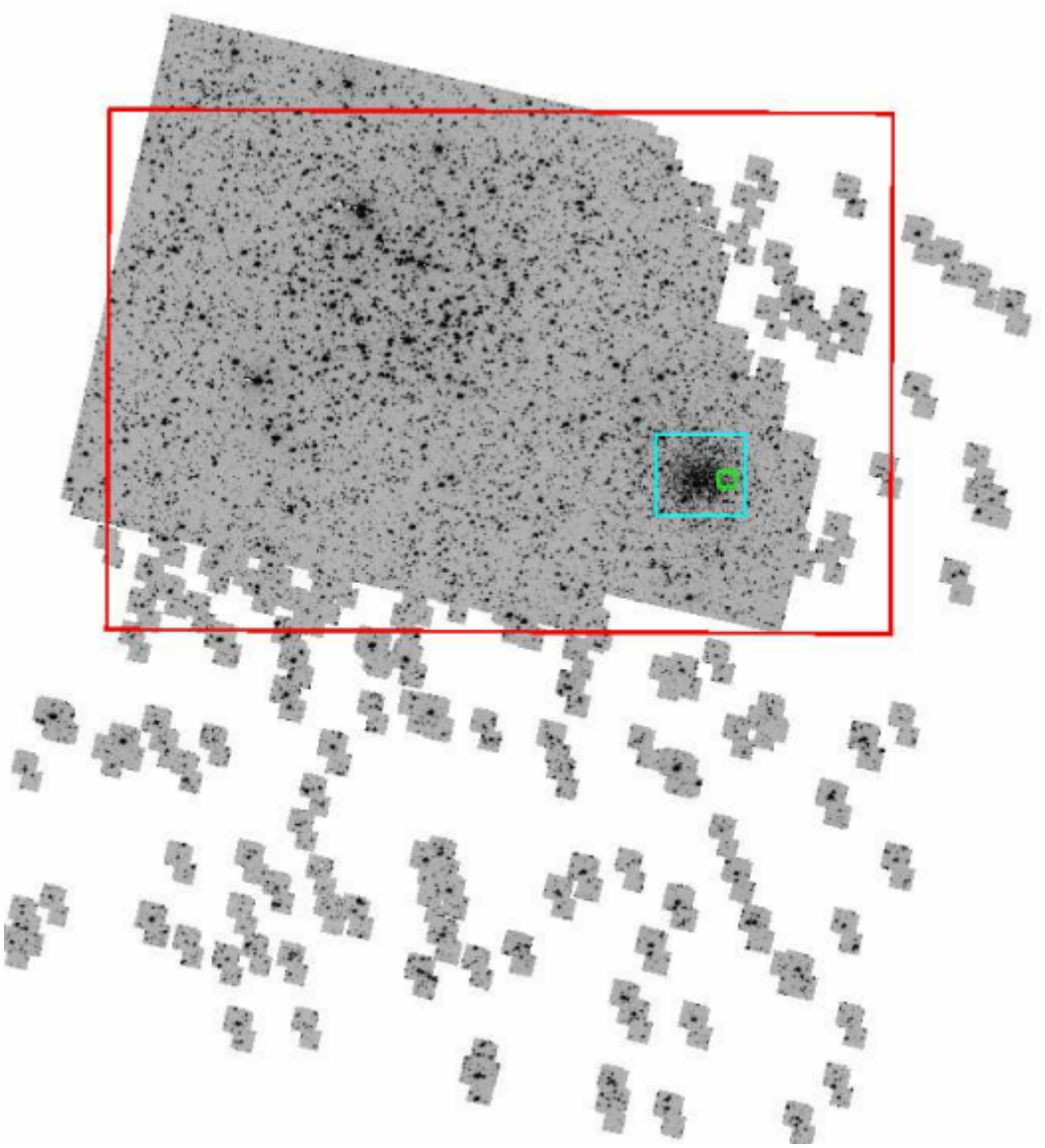

Figure 3.2: Example of full-frame image of *K2*/C0/channel-81 used in light-curve extraction. The red rectangle represents the field of view of the Schmidt input list (Nardiello et el. 2015). The cyan and green boxes point out different zoomed-in regions around NGC 2158 (Libralato et al. 2016a) shown in figure 3.4 for the zoom-in panels.

3.2 Reliable Modelling of PSF

K2 PSF is undersampled. The undersampled PSF needs to be modelled properly to measure position and flux of sources, otherwise wrong models can contribute to the analyzed source with systematic errors, especially while measuring flux and position of the source. Moreover, not corrected models may cause spurious residuals during the neighbour-subtraction phase of the light-curve extraction.

To model *K2* PSF, the authors used the effective PSF approach of Anderson & King (2000). The effective PSF is the convolution between the instrumental PSF and the pixel response and sensitivity. The effective PSF directly tell you how the flux of a star is distributed over the pixel in an image. This is what is needed to measure position and flux of all stars. However, undersampled PSFs suffer of a degeneracy between shape of the PSF and stellar positions that must be broken to model the PSF. To this task, dithered images, in which stars map different region of the pixels, are required.

Kepler calibration data is not public available. *Kepler* main mission data is not good for this task because the pointing was very stable and the stars were almost fixed in the same position. However, during *K2* mission the *Kepler* spacecraft is not able to keep a stable pointing after the failure of the two reaction wheels. Therefore, the stars move from one image to the next one and map different regions of the detector. For this reason Libralato et al. chose to use *K2*/C0 data itself to properly model the effective PSF of channel-81. However, since it is not matter of this thesis, I will leave the detailed description of the method to the paper of Libralato et al. (2016a).

The final result of the effective PSF model is a 21×21 array of points that covers 5×5 pixel^2 area. This is an average effective PSF for the entire *K2*/C0 that lasted for 75 days. However, there is no instrument that has a PSF that is so stable over time. If such average PSF was used for the neighbor subtraction, it would have left some residuals that could have harmed the flux measurement during the light-curve extraction. Therefore, Libralato et al. (2016a) chose to perturb the average effective PSF and take into account the temporal variation. Briefly, for each image they fit and subtracted the average effective PSF to all bright stars. Then they collected all the residuals and used them to adjust the PSF. This way they obtained one time-perturbed effective PSF for each *K2*/C0/channel-81 image to use to measure position and flux of all stars, and during the light-curve extraction. In figure 3.3 there is a comparison between a library effective PSF and a time perturbed effective PSF. The difference between the two PSFs is clear.

These effective PSFs were then used to fit the position and flux of all

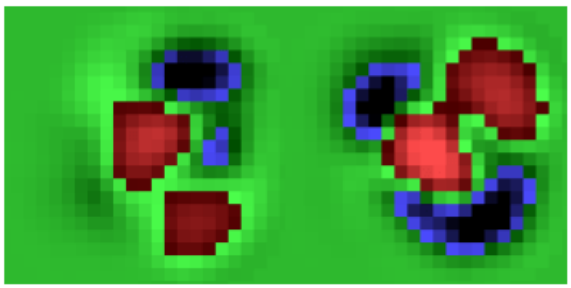

Figure 3.3: Comparison between the average effective PSF (left) and a perturbed effective PSF (right) (Libralato et al. 2016a).

sources in each *K2*/C0/channel-81 exposure. These stellar catalogs were used to link each *K2*/C0/channel-81 image to the high-angular-resolution input list during the light-curve extraction (see section 3.5).

3.3 Photometry in *K2* Images

Measuring photometry after neighbor subtraction provides more precise photometry on images than the original images (Nardiello et al. 2015), otherwise the lights coming from the neighbors could contribute to the flux of the observed object. After neighbor subtraction, aperture and PSF-fitting photometry can be better performed on the target star even in crowded environments as stellar clusters.

In order to get best photometric precision in *K2* images, accurate PSF models and a deep, complete input list need to be used (Nardiello et al. 2015). The *K2* PSFs were obtained as described in section 3.2. The input list cannot be obtained from *K2* images because of *Kepler* pixel scale ($\sim$4 arcsec pixel^{-1}). Therefore, Libralato et al. (2016a) used the input list made with another telescope with completely different angular resolution.

3.4 High Angular Resolution Input List

The input list has been created thanks to Asiago Schmidt Telescope. It is made by 75 935 objects measured without any filter (white light, hereafter N-filter magnitude; Nardiello et al. 2015). Using PSF fit, every source in the Asiago Input Catalogue (AIC) was obtained from the stacked image.

Comparing the Schmidt stacked Schmidt image with *K2* images, the Asiago Schmidt image provides higher resolution that makes it possible to find the location of the faint objects even in crowded environments such as that

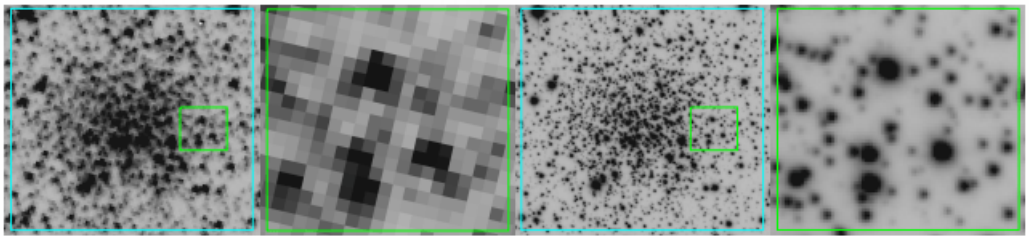

Figure 3.4: Comparison of two fields from *K2* (left two panels) and Schmidt stacked image (right two panels; Libralato et al. 2016a).

close to NGC 2158. In figure 3.4 a field close to NGC 2158 center is shown in a *K2* exposure and in the Asiago Schmidt stacked image with two different zoom-in levels. Basically, it is hard to find faint objects in the presence of nearby stars whose flux pollutes the pixels if low-angular-resolution images are used.

3.5 Light-Curve Extraction

With all the previous ingredients, it is possible to extract light curves for all stars in the high-angular-resolution input catalog using PSF and aperture photometry with different apertures (1-, 3-, 5-, 10-px radius). This process can be briefly explained as follows. For each object in AIC, Libralato et al. (2016a) computed six-parameter linear transformations to convert the AIC location of these targets into each *K2* image reference frame. Only well-measured and bright neighbours of objects in 100-pixel radius area were used to compute the parameter of the transformations. If in this area there were not at least ten stars as neighbors, then the area needed to be increased.

They extracted the light curves from the original and from the neighbor-subtracted images. In the latter case, all close-by stars to a given target were subtracted from the image before to measure its flux. Each AIC object was measured with four different aperture sizes (1, 3, 5, 10-pixel radius) and also with PSF-fitting photometry.

3.6 Light-Curve Detrending

Unstable pointing of the *Kepler* spacecraft after failures result in an effect coming from its drift movement every 6 hours. Due to a non-perfect flat-fielding, when the star moves across different pixels on the CCD it experiences different intra- and inter-pixel sensitivity variations. These effects therefore

correlate with the position of the star. To correct (detrend) these effects, Libralato et al. (2016a) used all exposures of channel-81 obtained from C0, also those in the first part of the campaign. Some papers used different approach to correct this effect, e.g., self-flat-field method of Vanderburg & Johnson (2014), or the Gaussian approach of Aigrain et al. (2015). In this work (Libralato et al. 2016a) they used a look-up table of corrections, applied using a bi-linear interpolation. In figure 3.5, 3.6 and 3.7 there are some examples of the raw and corrected light curves.

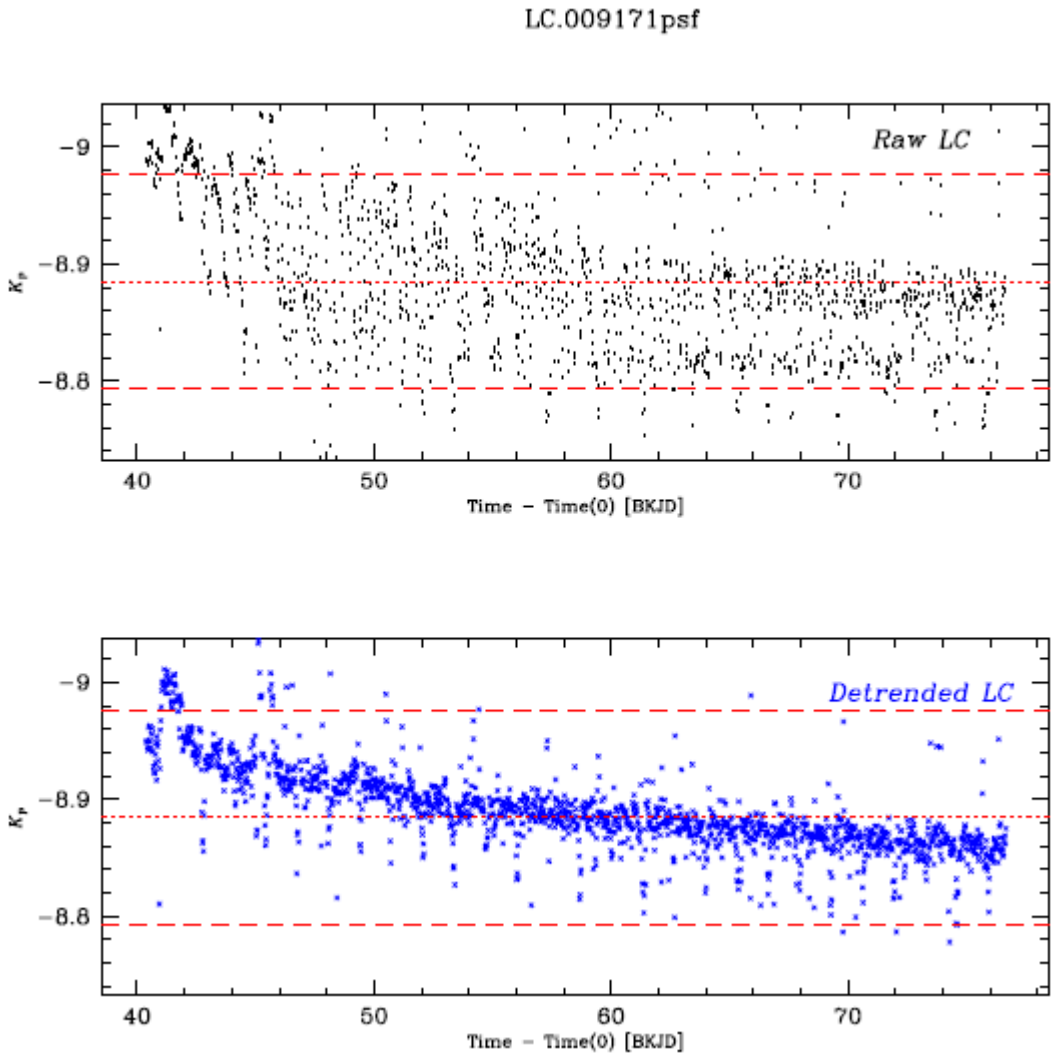

Figure 3.5: Comparison of the raw and corrected light curve of star #9171 obtained with PSF photometry. The period on the x-axis is given in days. Horizontal red dashed lines are set at $\pm 3.5\sigma$ around the median value (horizontal red dotted line).

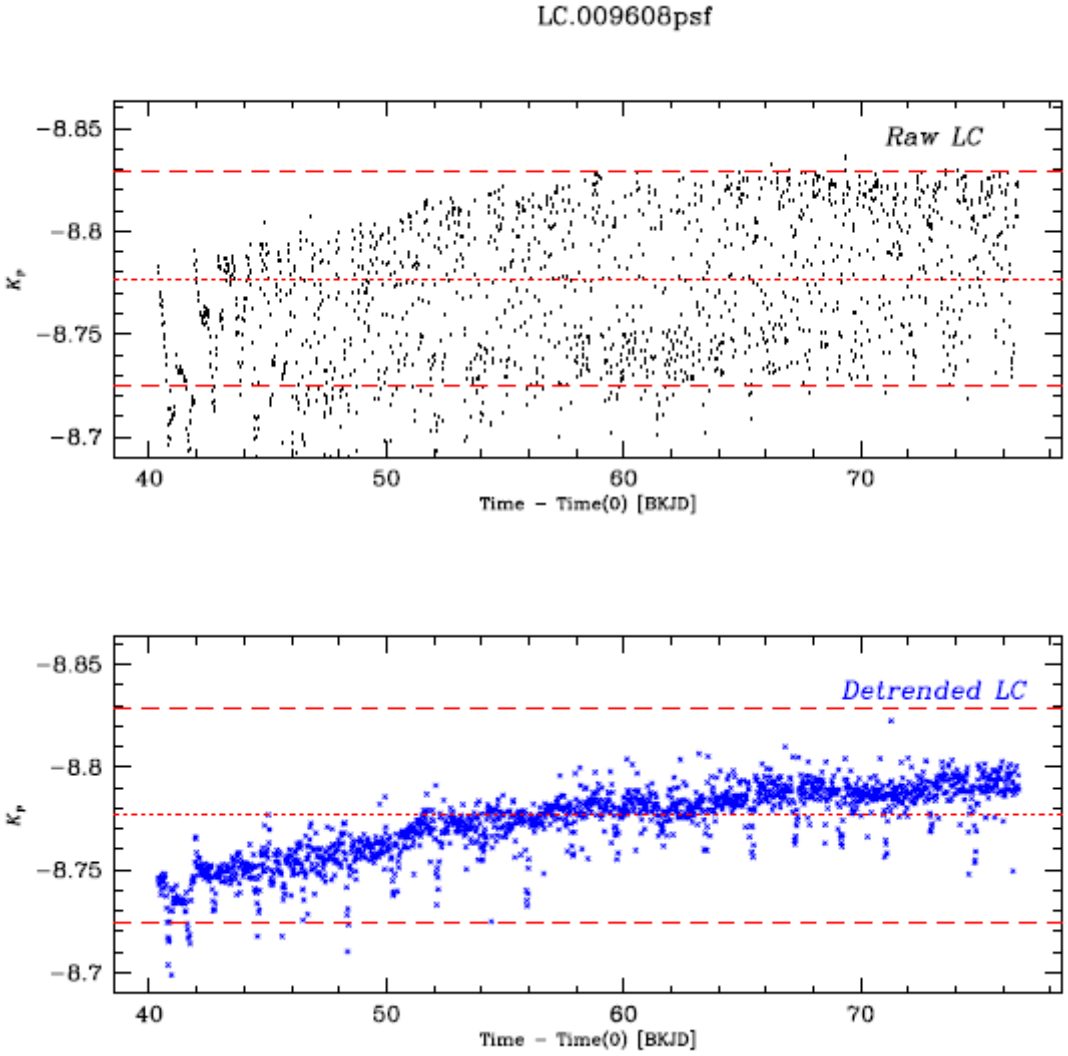

Figure 3.6: Comparison of the raw and corrected light curve of star #9608 obtained with PSF photometry.

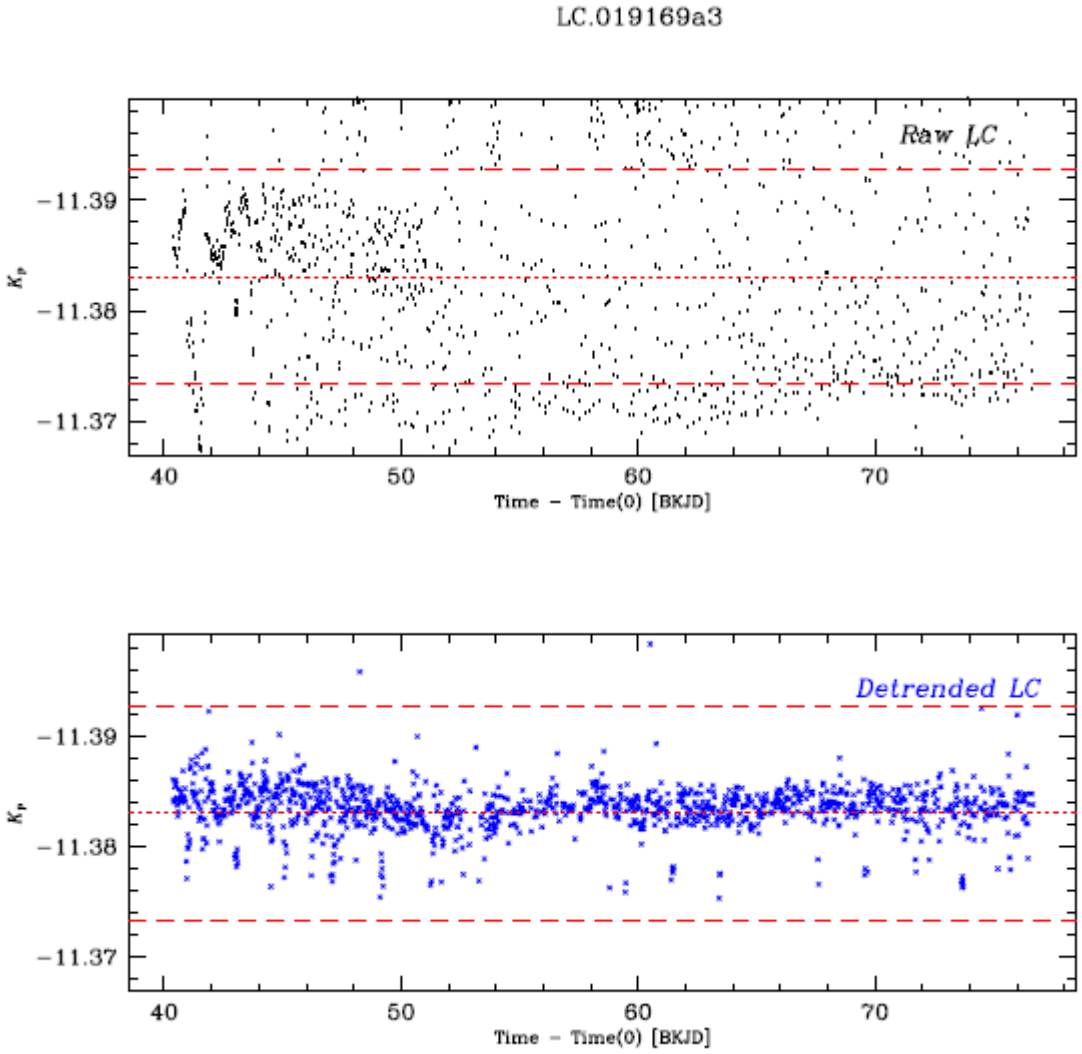

Figure 3.7: Comparison of the raw and corrected light curve of star #19169 obtained with 3-pixel aperture photometry.

Chapter 4

SEARCH FOR EXOPLANET

Chapter four is going to be about the process of finding exoplanets. My aim is to search for exoplanets in crowded environments in open clusters M 35 and NGC 2158. I start by chosing the best photometric method to search for the possible exoplanet signals. Then I explain which process and methods are used to get the exoplanet signal. Finally I present some possible exoplanet and eclipsing binary candidates and how their light curves look like. Also, I explain whether these exoplanet candidates are genuine or not.

4.1 Sample Creation

For each usable light curve, we selected the photometric method that shows, on average, the best photometric precision in the corresponding magnitude interval. We used the 6.5h root-means-square (rms), a kind of rms measured from the light curve after all features with the duration longer than 6.5h where removed from the light curve using a running-median filter of 6.5 hour window.

For bright stars aperture photometry works better. However, PSF photometry performs better on faint stars. I found that, 5- and 10- pixel aperture photometry works better than 3-pixel photometry for very bright stars. Also, PSF and 1-pixel aperture photometry performs better than 3-pixel aperture photometry for faint stars. In figure 4.1 there is a representation of 6.5-h rms for different size of the apertures as a function of *Kepler* and N-filter (Asiago Schmidt) magnitude. As shown in top of figure 4.1, for $N > -12.4$ PSF-based and 1-pixel aperture photometry work better than 3-pixel aperture photometry, while for $N < -12.4$ 3-pixel aperture photometry performs better than the previous two methods. In bottom panel of figure 4.1 there is the same plot as on top but in calibrated $K_{\rm P}$ magnitude to allow the reader

a comparison with other published works on this topic.

4.2 Light-Curve Preparation and Outliers Clipping

The detrended light curves may have outliers and long-term effects (systematic or intrinsic variability) that could harm the detectability of exoplanet candidates. Therefore, the second thing we made was to remove them.

To get rid of these problem, we modeled long-term systematics and variability of the star using a 3th-order spline with 150 break points. Then we subtracted this model to the light curve. This step makes it possible to better detect any significant flux drop due to a planet or an eclipsing binary.

As described in Libralato et al. (2016a), thruster-jet-related events were removed from the light curves, as well as the first 30 days of *K2*/C0 where the pointing was very unstable. I will refer to these light curves as clean light curves. Then I removed most of the outliers that were left in the light curve.

These outliers may harm detectability of possible exoplanet signal, therefore that they need to be clipped carefully otherwise signals due to exoplanets could be lost. We proceeded as follows: we divided the light curve in several bins and in each bin we computed median and 68.27-th percentile around the median values. I excluded from the subsequent analysis all point that, in each bin, were 3.5 σ brighter or 15 σ fainter than the median value. After this process, I obtained light curves hereafter called as flat light curves.

4.3 BLS Periodogram and Normalization

After obtained the flat light curves removing outliers, we used Box-Least-Squares (BLS) periodograms (Kovacs et al. 2002) implemented in VARTOOLS program (Hartman and Bakos, 2016) to find transit-like events. BLS is particularly effective in finding box-like flux drops in the light curves. For each flat light curve, we applied BLS to find possible signals with periods in the range of 0.5 and 75 days. Totally there were 54 922 light curves and therefore obtained the same number of periodograms. Furthermore, we normalized all periodograms to get rid of possible spurious detections in the long-period regime as described in Vanderburg et al. (2016). Then we iteratively chosed the highest peak in periodograms that means the periods that produce the highest Signal-to-Noise Ratio (SNR), while removing false frequencies around 6.5h or multiples as described in Libralato et al. (2016b) and Nardiello et al. (2016).

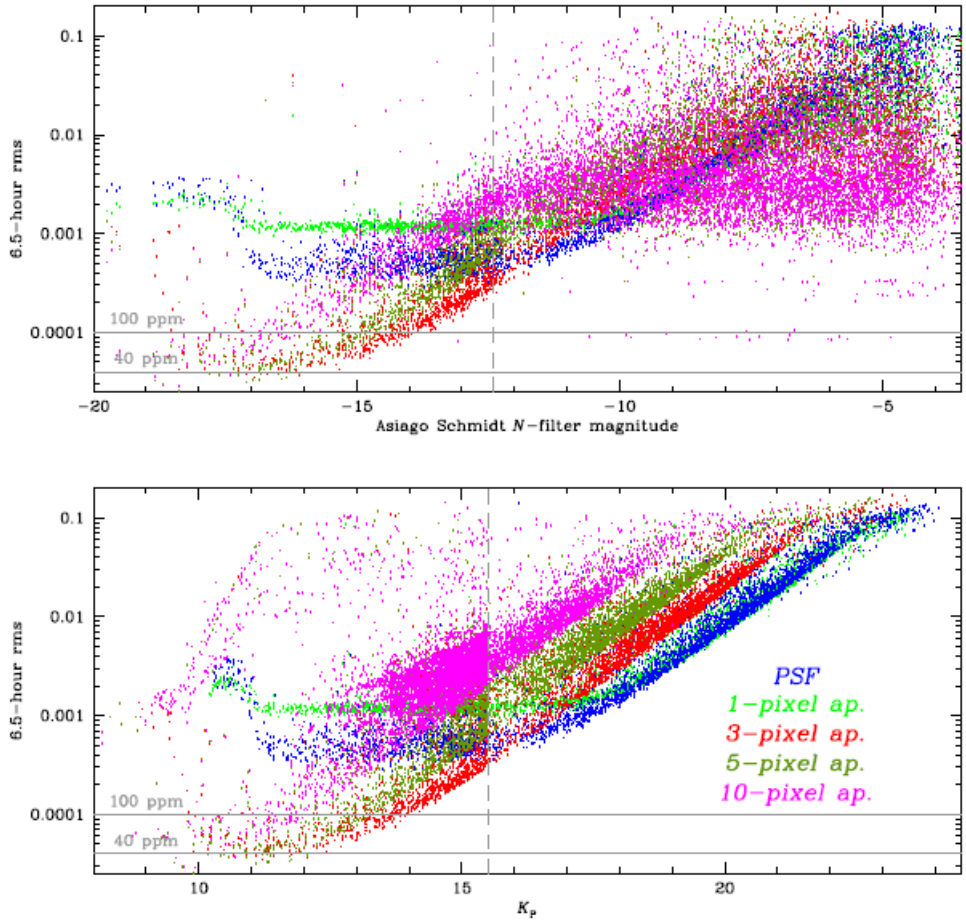

Figure 4.1: 6.5h rms as a function of the N-filter (Asiago Schmidt) magnitude (top) and calibrated $K_{\rm P}$ magnitude (bottom) for each photometric method. The grey, dashed vertical line shows the limit at which PSF and 1-pixel aperture photometry perform better than the other photometric methods (faint stars).

We then phased the light curves with such periods and visually inspected them to detect any significant boxy-like shape referable to a planetary transit.

4.4 Light-Curve Analysis

To better analyze the 54 922 light curves, I have divided them into 15 groups of 5000 light curves each.

Since we cannot visually inspect all light curves, we chose to select those that showed a high SNR value for the highest peak in the periodograms. A high-SNR peak in the periodogram indicate the presence of a significant box-shape signal in the light curve with that period.

In figure 4.2 I plotted for the first group of light curves the SNR versus period previously detected within the normalized periodograms of each light curve. We selected by-hand the curves to analyze to get rid of the light curves which highest peak in the periodogram was not high enough with respect to the bulk of the points. Of course this is a compromise between to do not visually inspect all light curves and miss some objects with boxy-flux drops with a low SNR in the periodogram. In figure 4.2 the red line is my by-hand selection threshold. After this selection, I had about 100 light curves. I visually inspected each of them carefully. I also excluded eclipsing binaries. Furthermore, for each eclipsing binary I checked the *K2* variable catalog (Libralato et al. 2016a) to check if it was a new discovery. The light curves that show boxy-like flux drops were saved as possible exoplanet candidates for further analysis. At the end of the by-eye analysis of all light curves, totally 6 light curves were promising for an exoplanet search. The others were marked as eclipsing binary or variables. In figures from 4.3 to 4.8 these clean and phased light curves can be seen.

4.4.1 Checking Close Variables

To understand if these six exoplanet candidates were genuine, I have looked for close variable of these stars using *K2* variable catalog (Libralato et al. 2016a) which contains 2849 variables. In the first iteration I searched within 20 *Kepler* pixels from each candidate to find eclipsing binaries that could mime transit events. Then I looked within 43 *Kepler* pixels (nearly 200 Asiago Schmidt pixels). In figures from 4.9 to 4.12, top panel these close variables can be seen in the field. Carefully checking each candidate even with period of the close variables, it could be possible to understand that only two of them were sufficiently isolated. In figures from 4.9 to 4.12, on the bottom panel I show a comparisons between the closest variable and

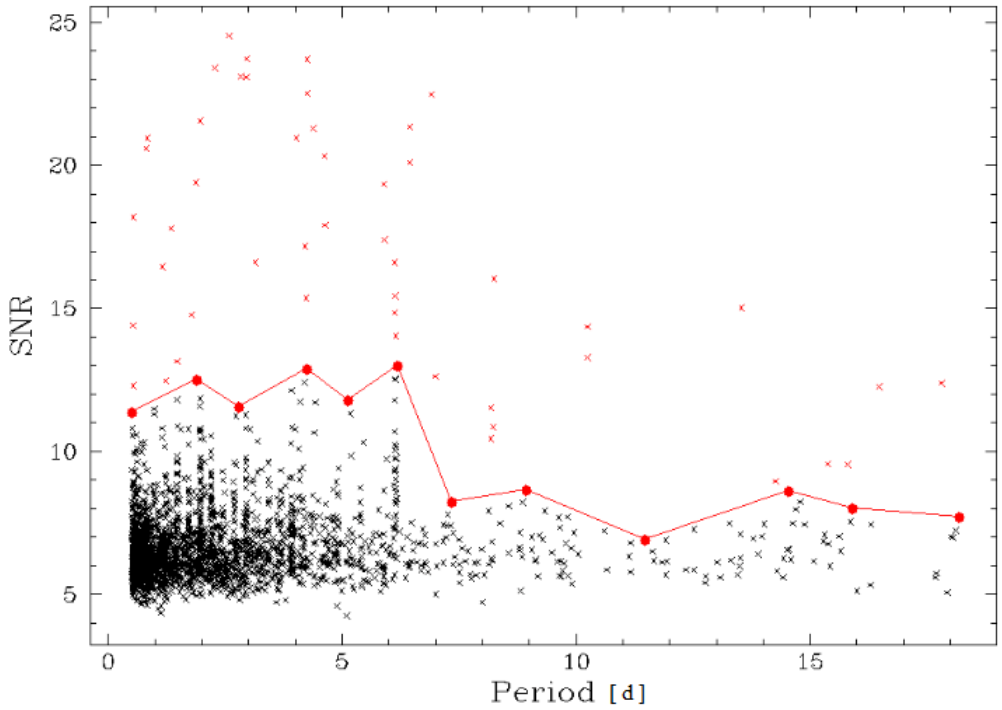

Figure 4.2: SNR as a function of the period of the first 5000 clean light curves. Red line represents the threshold of by-hand selection. Red points above the threshold were analyzed.

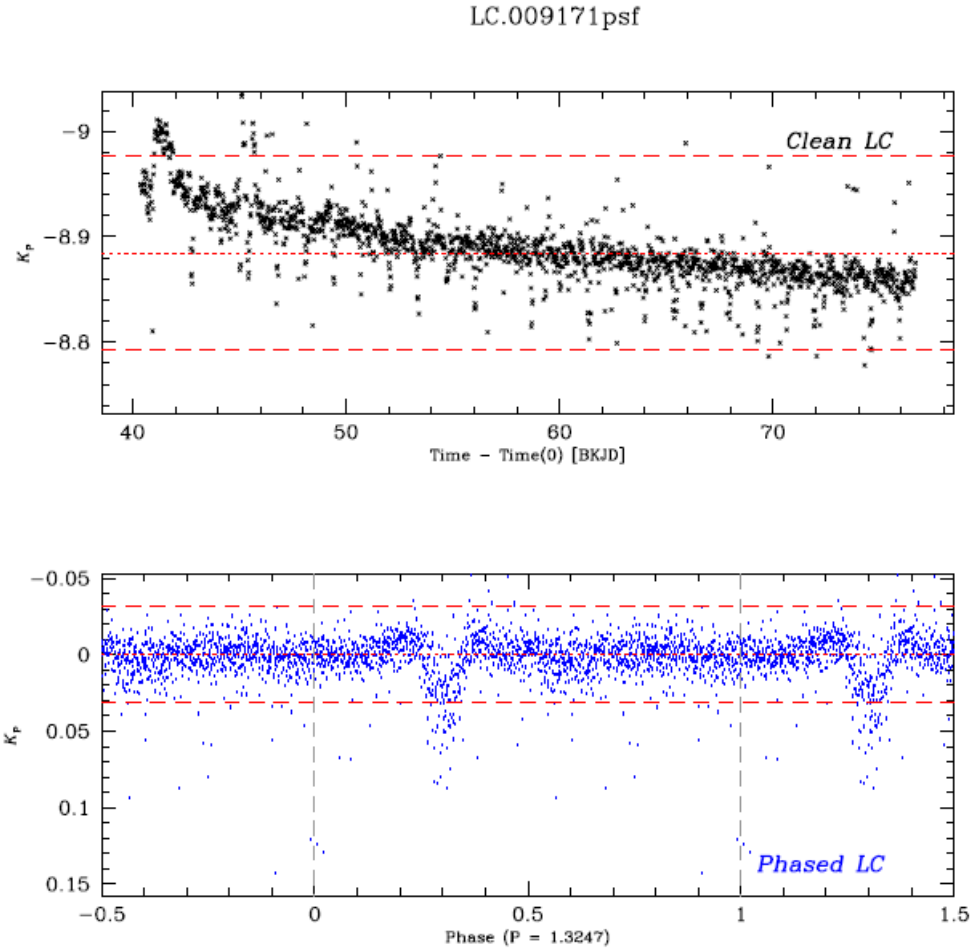

Figure 4.3: The clean light curve (top) and the phased flat light curve (bottom) for star #9171 (the period on the x-axis is given in days). The "V"-shape flux drop and its depth suggested a possible eclipsing binary.

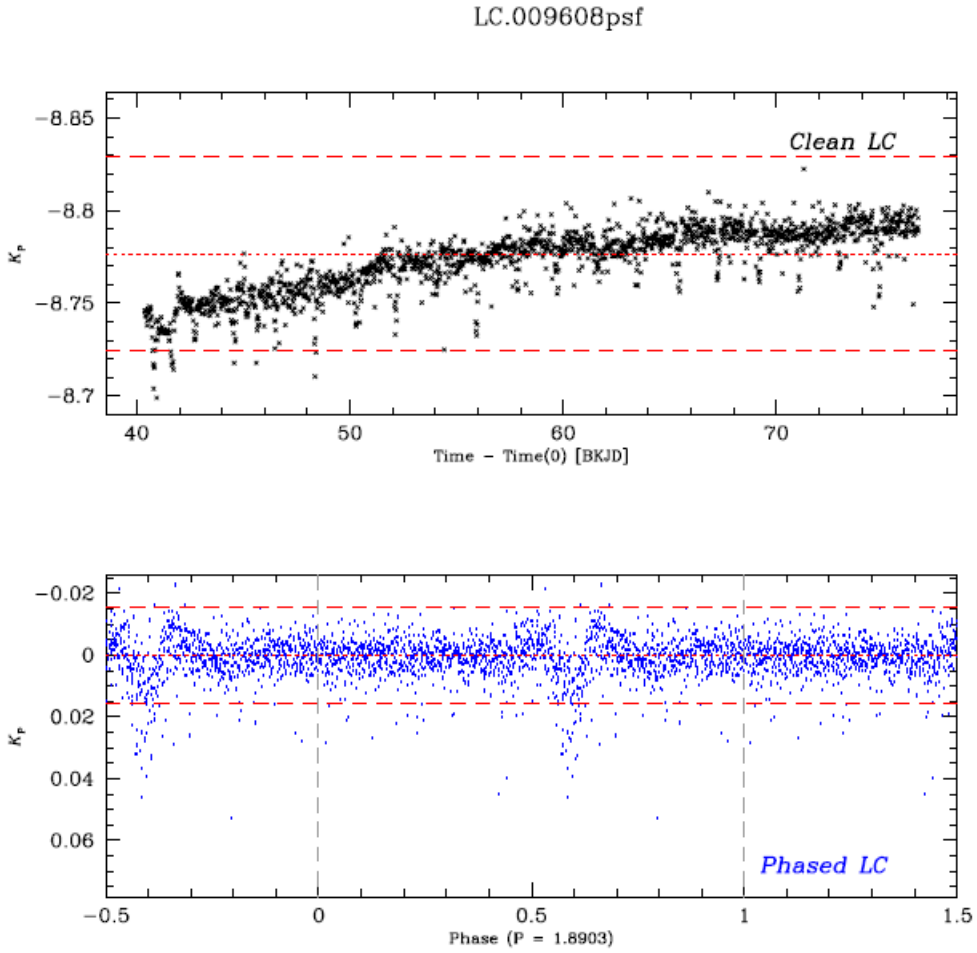

Figure 4.4: Same as in figure 4.3 but for star #9608.

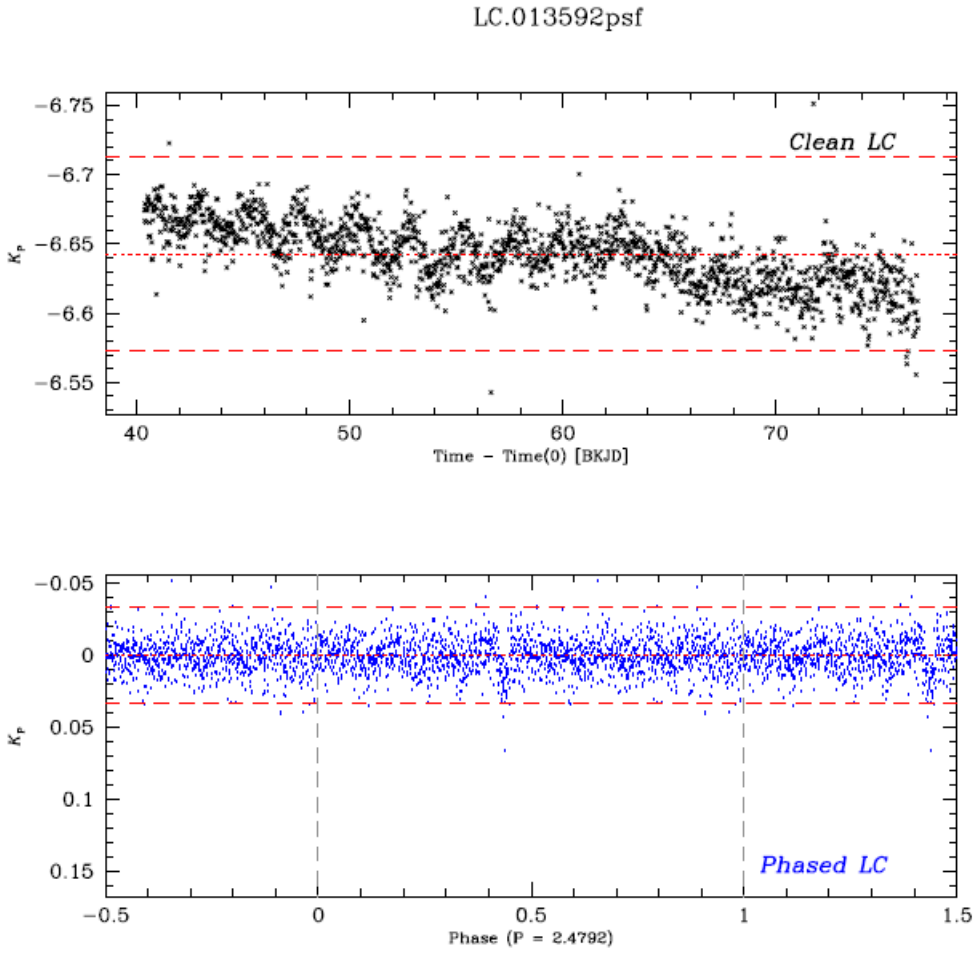

Figure 4.5: Same as in figure 4.3 but for star #13592.

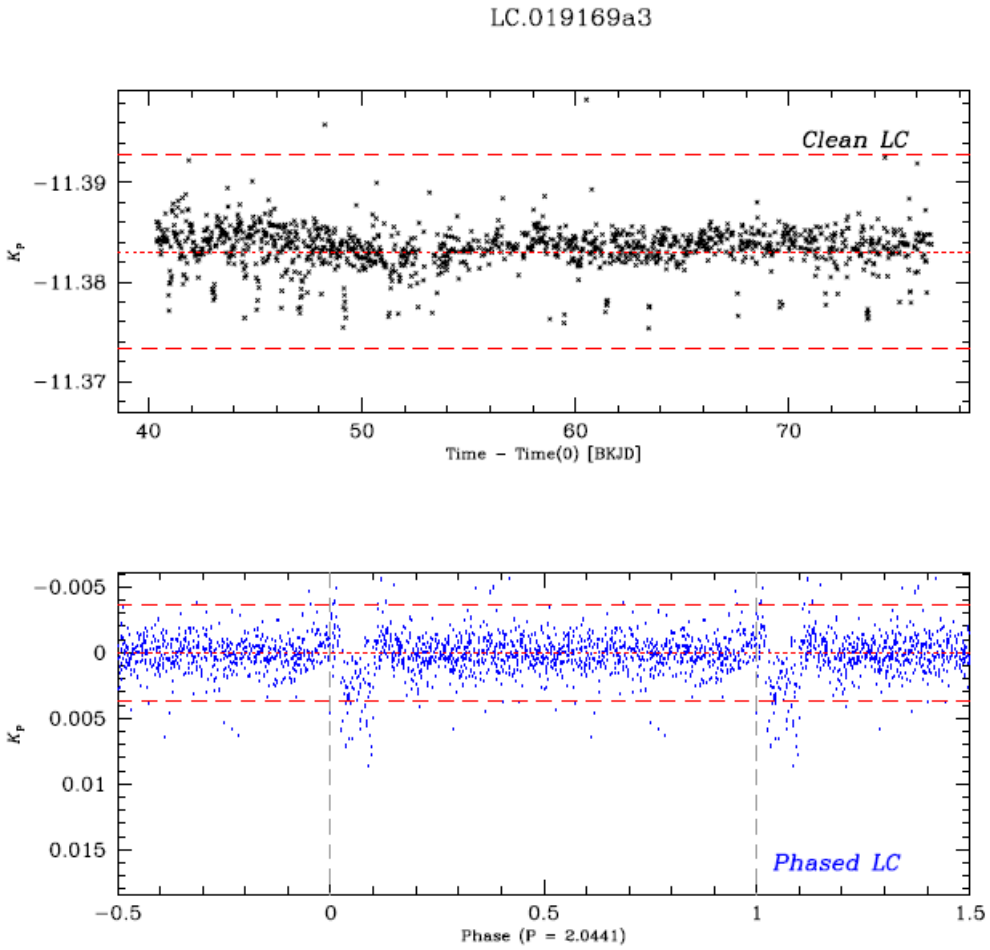

Figure 4.6: Same as in figure 4.3 but for star #19169. Period of the star is consistent with 2.04-day periodicity effect.

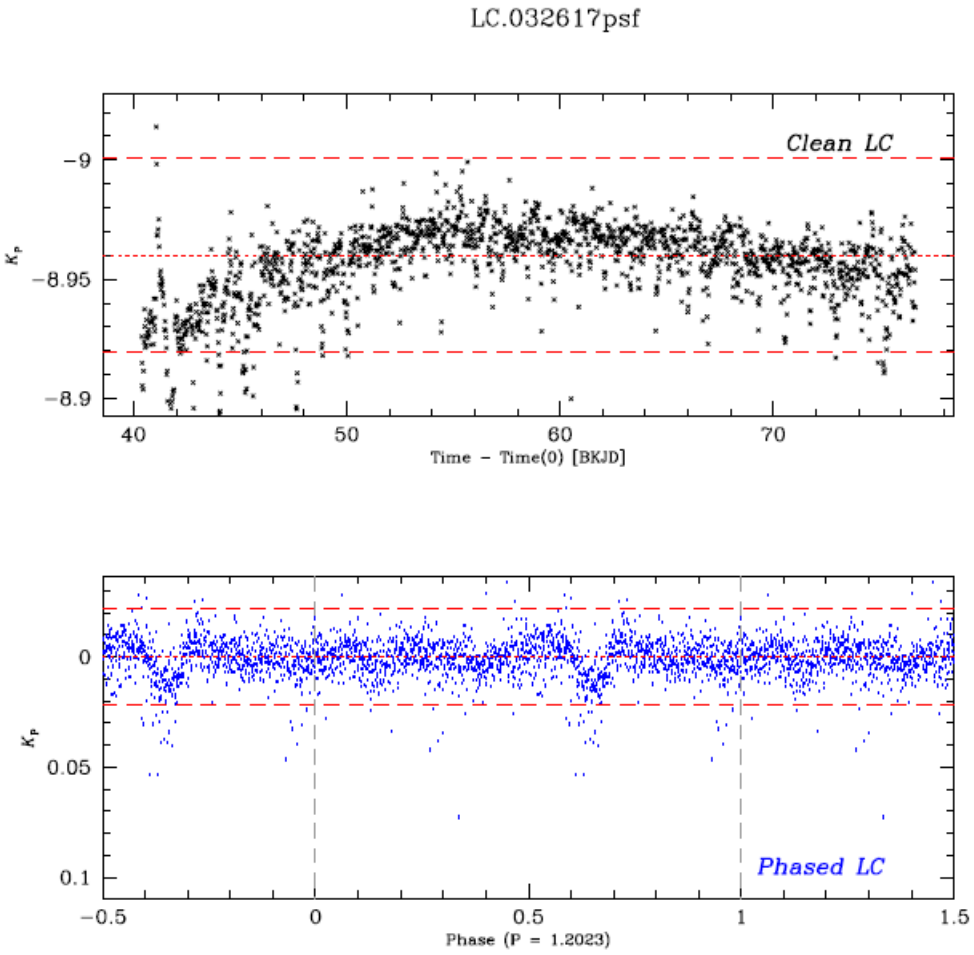

Figure 4.7: Same as in figure 4.3 but for star #32617.

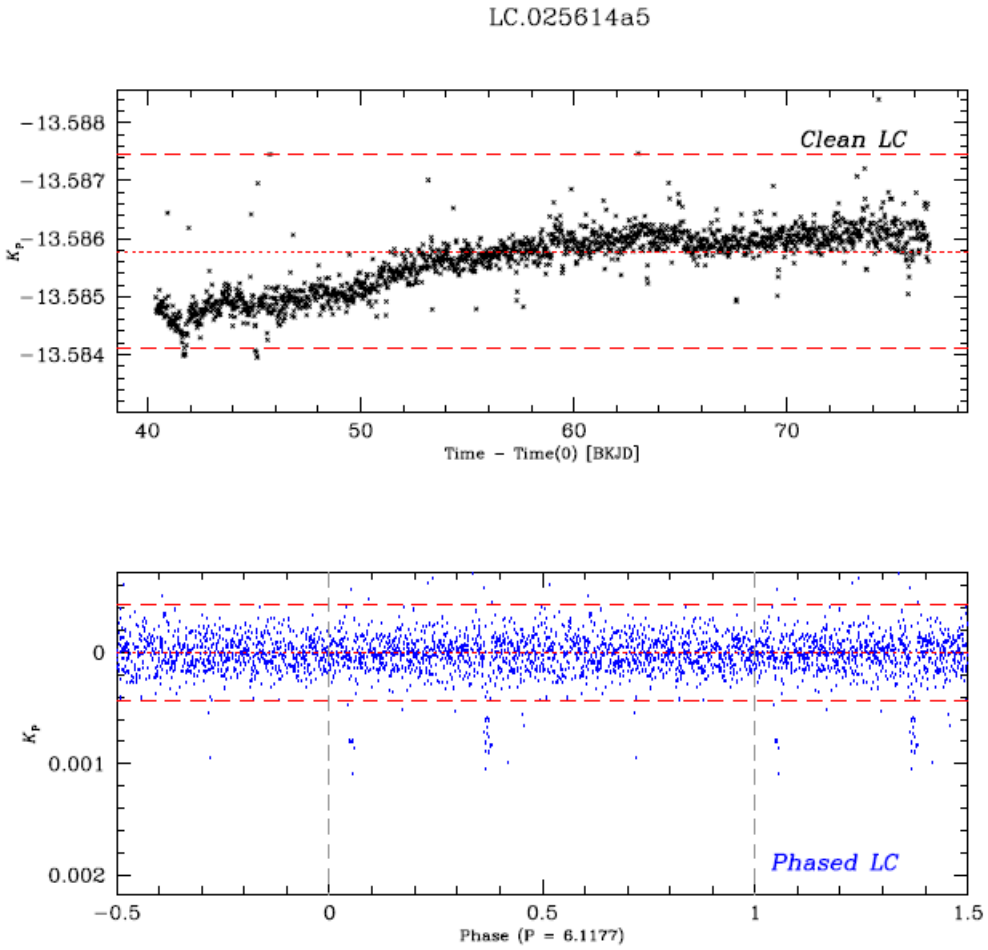

Figure 4.8: Same as in figure 4.3 but for star #25614. Period of the star is three times of 2.04-day periodicity effect.

possible host star. At the end of the process only two remaining possible exoplanet candidates were left.

As can be seen in the figure 4.13 these two remaining light curves, LC.019169 and LC.025614 show a flux drop every 2.04 days or multiple of this value. Although they were good candidates after lots of processes, some of the light curves still show flux drops periodically that look boxy-like transits with periods 2.04 days (Libralato et al. 2016a). Not all stars exhibited this kind of drop that could be a column-related over-correction of the *Kepler* pipeline. This effect could be also caused by firing of jets every two days for the momentum dump (Howell et al. 2014; Lund et al. 2015). Due to lack of detailed knowledge about this effect, it cannot be corrected easily and there could still be a trace in the periodogram (as shown by Libralato et al 2016a). Although it has some drawbacks, it makes possible to separate these events from genuine eclipses/transits. Therefore, my last two candidates did not survive since they were not real transits.

4.5 A New Sample Selection

In the previous analysis we used BLS to make the periodogram for each light curve, and we selected the period with respect to the highest SNR, excluding all peaks related to the 6.5h thruster-jet fires. However, as shown in the previous section, there is also a 2.04-day periodicity. Therefore we repeated the entire procedure excluding also these periods when selecting the peak in the periodograms in order to increase the number of possible targets.

In figure 4.14 I plot SNR versus period for 5000 light curves obtained with the previous procedure described in section 4.4 (left panel) and with the new method described here (right panel). However, there are still some spikes possibly caused by firing of jet in every 6.5 hours and also the periodicity effect of 2.04 days. In order to analyze more stars, I have also put a flat SNR threshold at nine, as can be seen in figure 4.14 (red line). By doing this, I obtained 2481 light curves, out of 54 922. I have analyzed all these light curves visually inspecting them and I excluded those already contained in the *K2* variable catalog of Libralato et al. (2016a). After these checks, only 130 objects were left. Then I have cross checked this list with my previous light-curve list which was obtained as described in section 4.4. I found that 36 light curves were also contained in the previous list and therefore I removed them. I have checked the remaining 94 light curves in terms of transit depth (to exclude eclipsing binaries), close variables, periodicities and possible mirror effect that could be caused by the other stars.

After these procedures, I found that three objects showed in their light

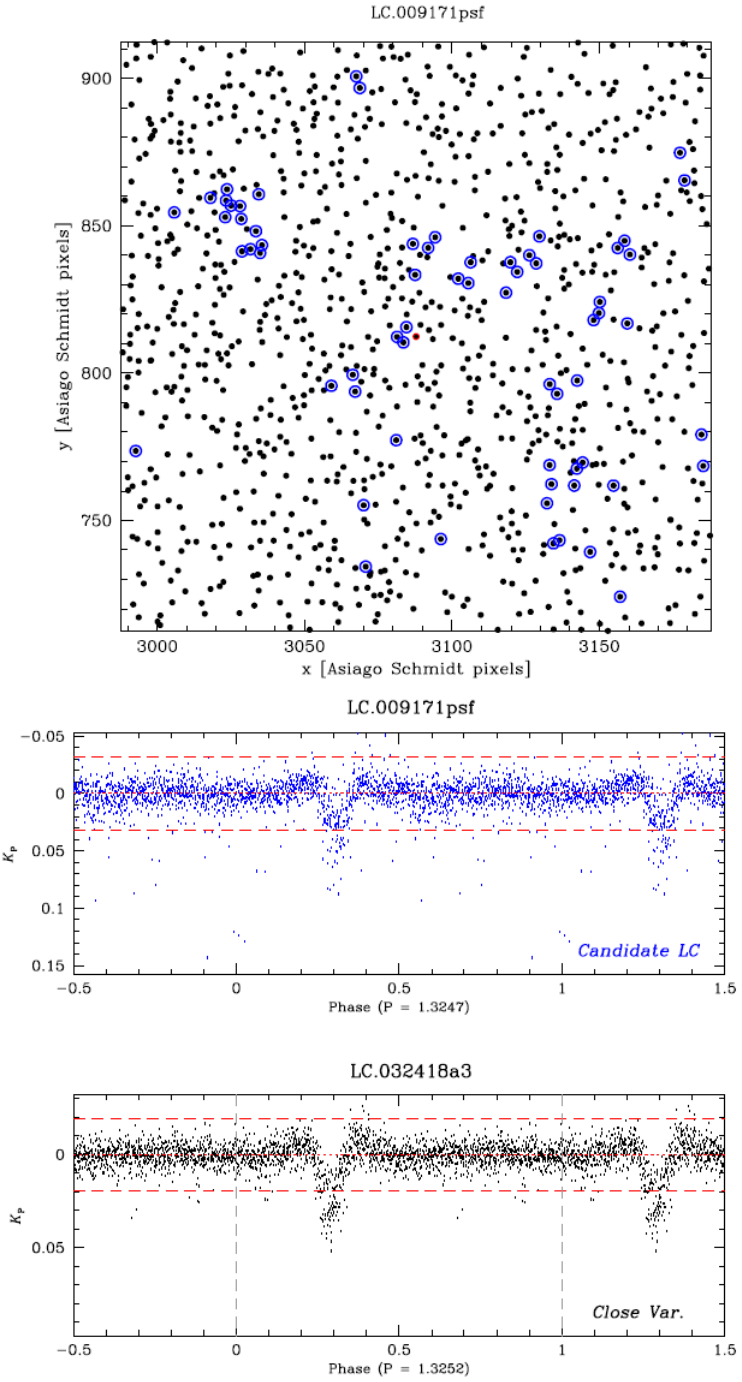

Figure 4.9: On the top panel, the black dot with red circle represents the possible candidate, while black dots with blue circles represent the close variables. There are 3 close variables nearby. On the bottom panel, there is a comparison between star #9171 and its closest variable star #32418. It can be seen that periods (on the x-axis is given in days) of these two stars are nearly the same and they show almost the same amount of flux drop. They probably are just eclipses due to close variables.

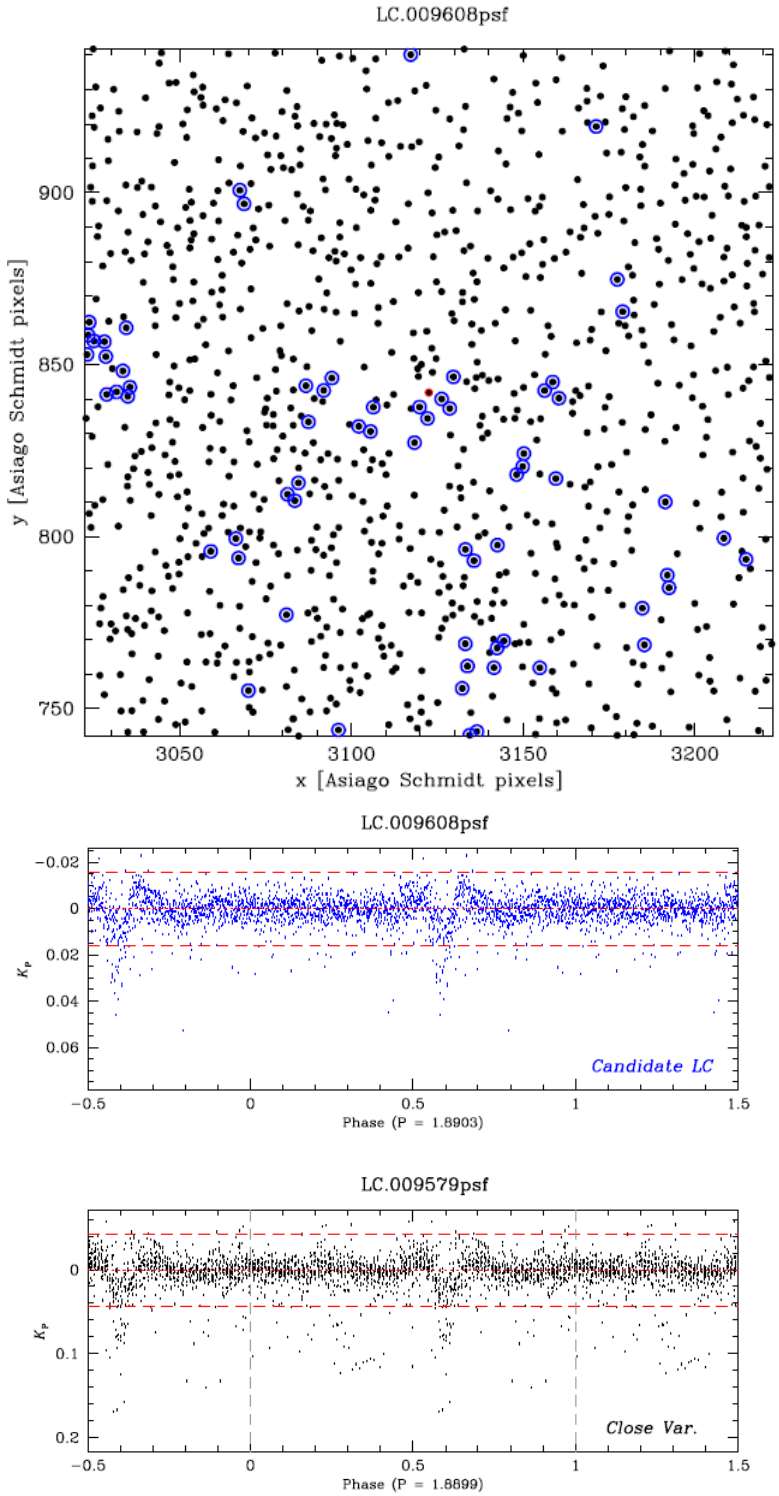

Figure 4.10: Same as in figure 4.9 but for star #9608.

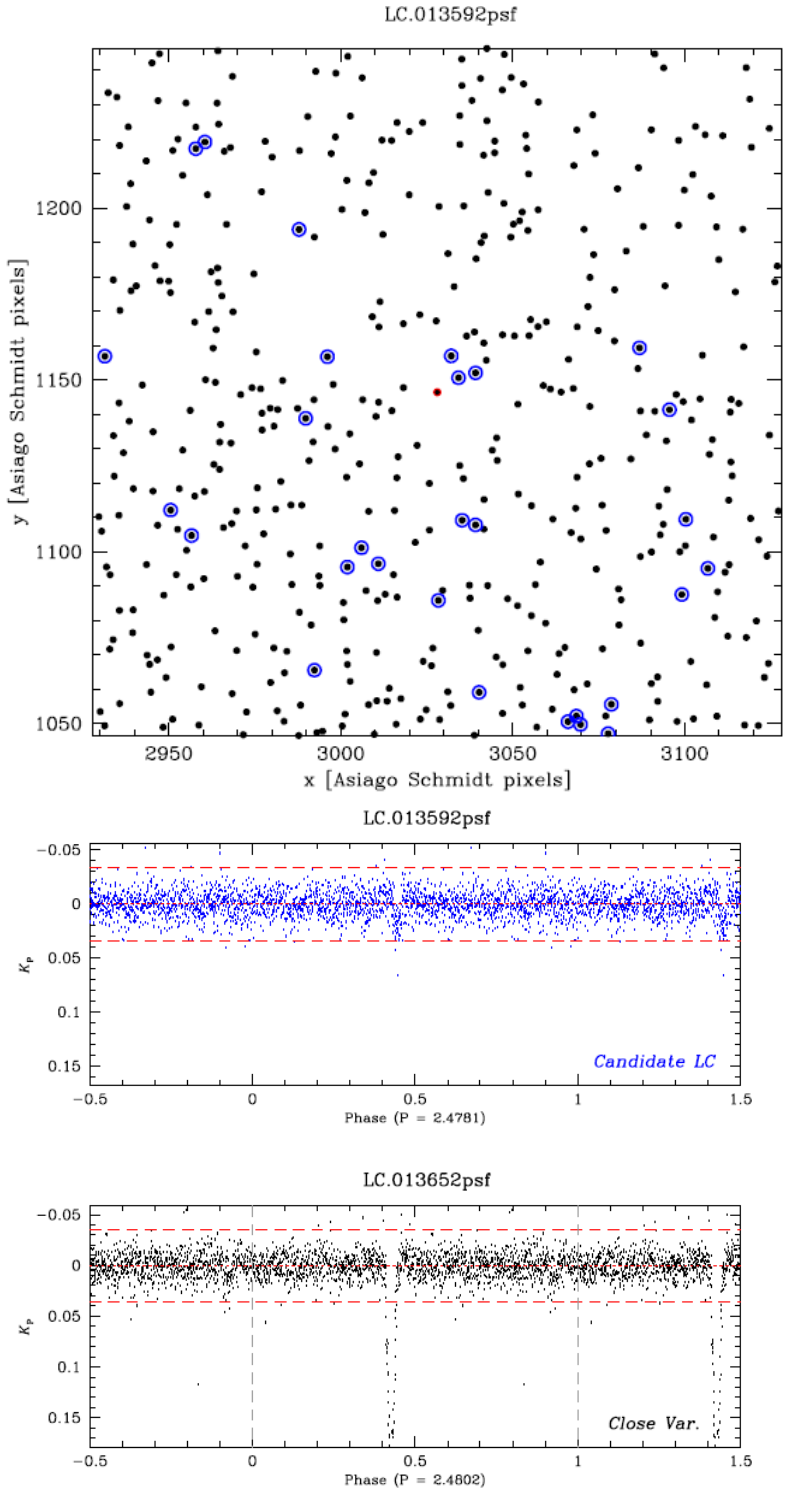

Figure 4.11: Same as in figure 4.9 but for star #13592.

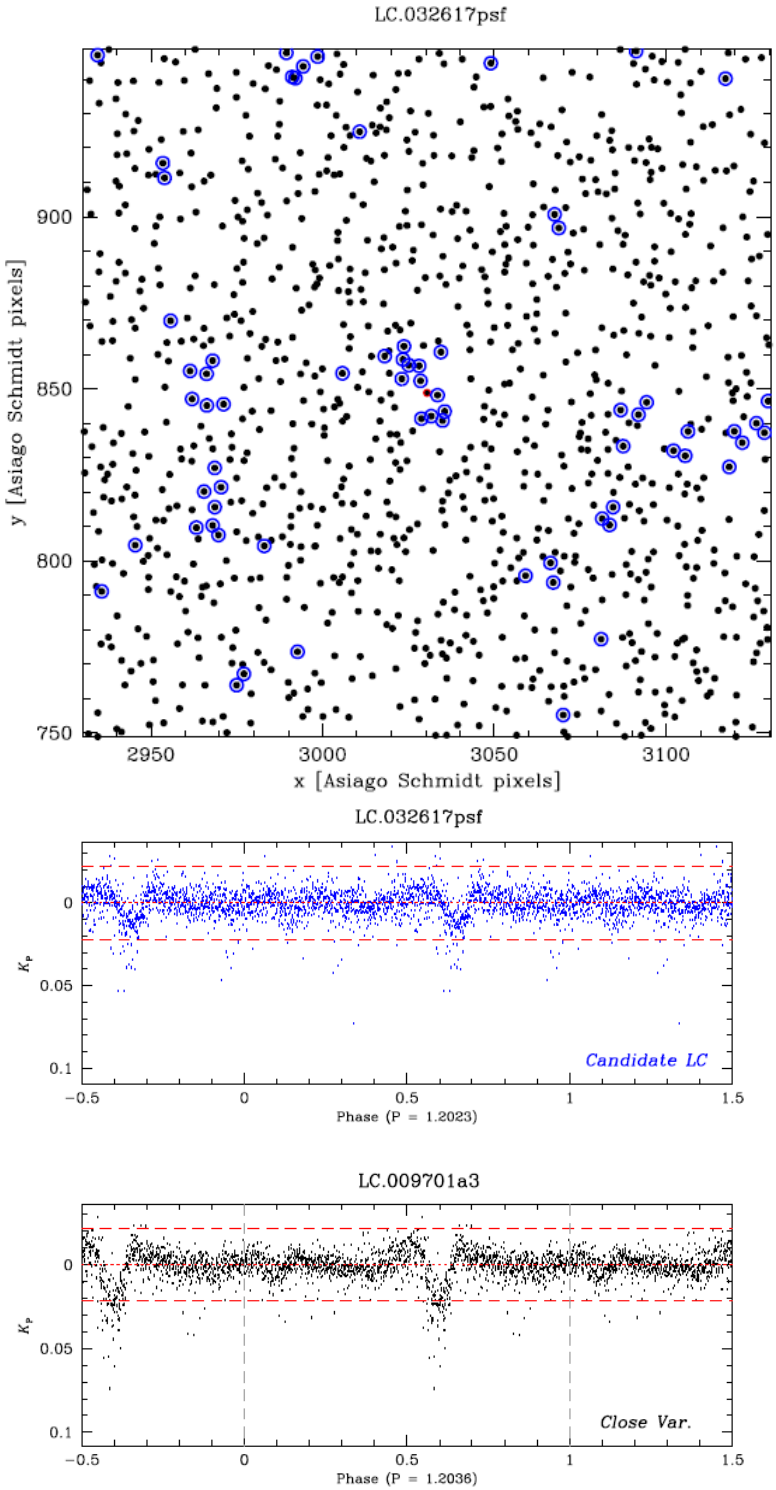

Figure 4.12: Same as in figure 4.9 but for star #32617.

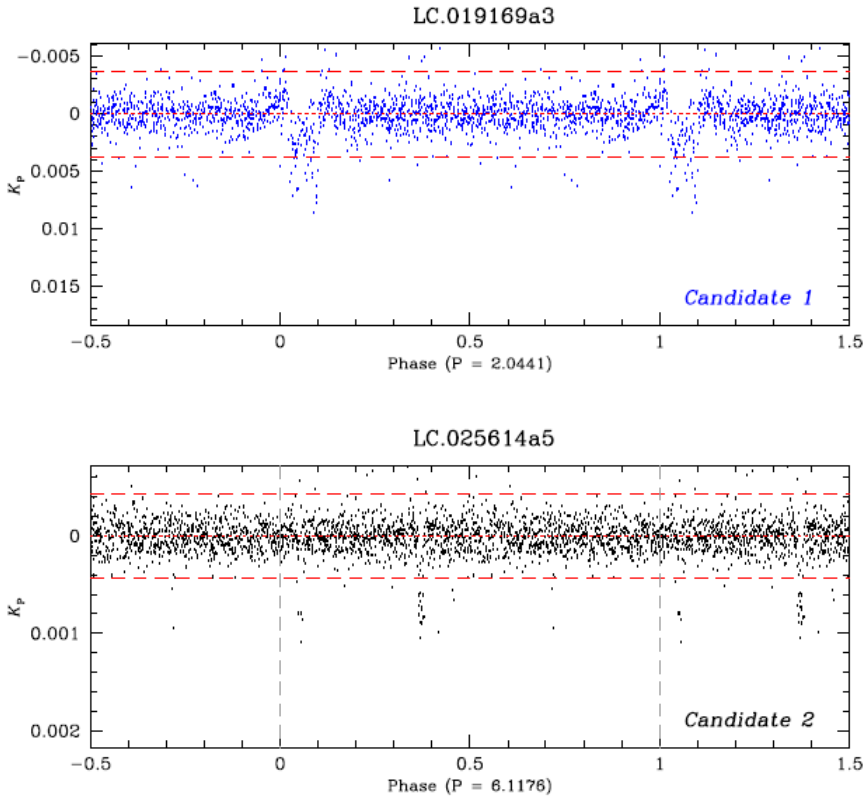

Figure 4.13: Star #19169 is showing 2.04-day period, while the period of the star #25614 is three times 2.04 day. These flux drops are just the effect of the 2.04-day effect.

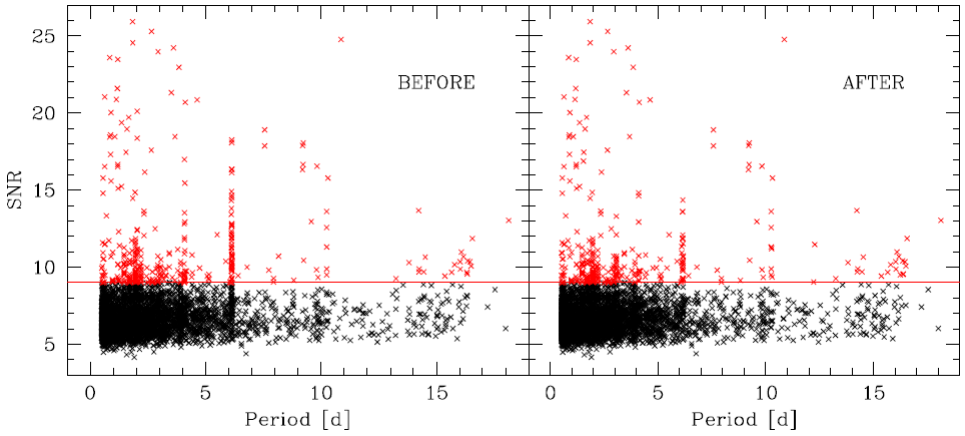

Figure 4.14: SNR as a function of period for a sub-sample of the clean light curves. To get rid of the spikes and 2.04-day effect, and to avoid to analyze light curves with a low probability to present box-like signals, the threshold (red line) is put at SNR=9.

curves the 2.04-day periodicity effect, 79 of them were eclipsing binary or very close to them and the remaining 12 stars were promoted to exoplanet-host candidates. In figures from 4.15 to 4.25, 10 out of 12 of these light curves can be seen.

Analyzing more in detail these objects, I found that the flux drops in their light curves were just noise, or due to eclipsing binaries or systematic effects. The remaining two light curves (LC.007139 and LC.026448) survived after these tests and were further studied.

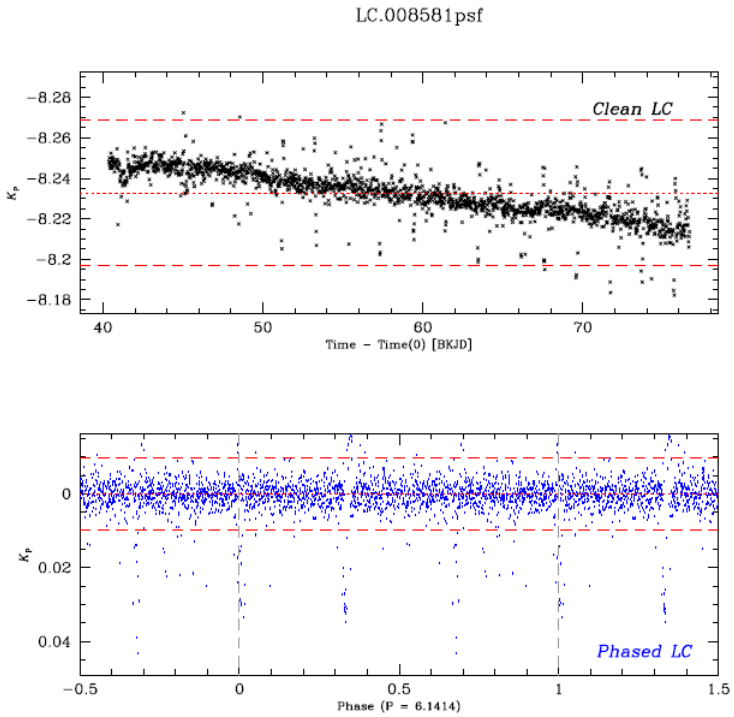

Figure 4.15: Clean light curve (top) and flat light curve phased with the period (on the x-axis is given in days) found in the analysis (bottom) for star #8581.

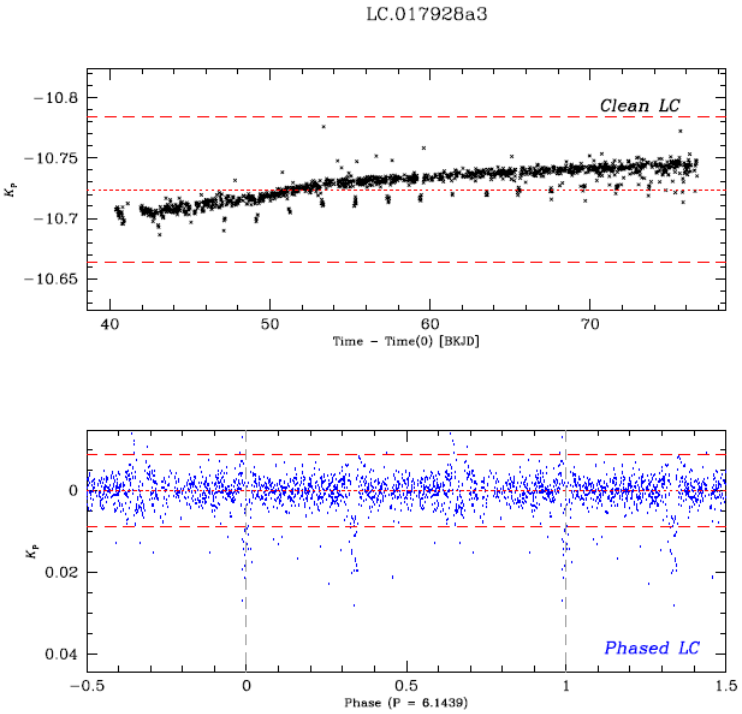

Figure 4.16: Same as in figure 4.15 but for star #17928.

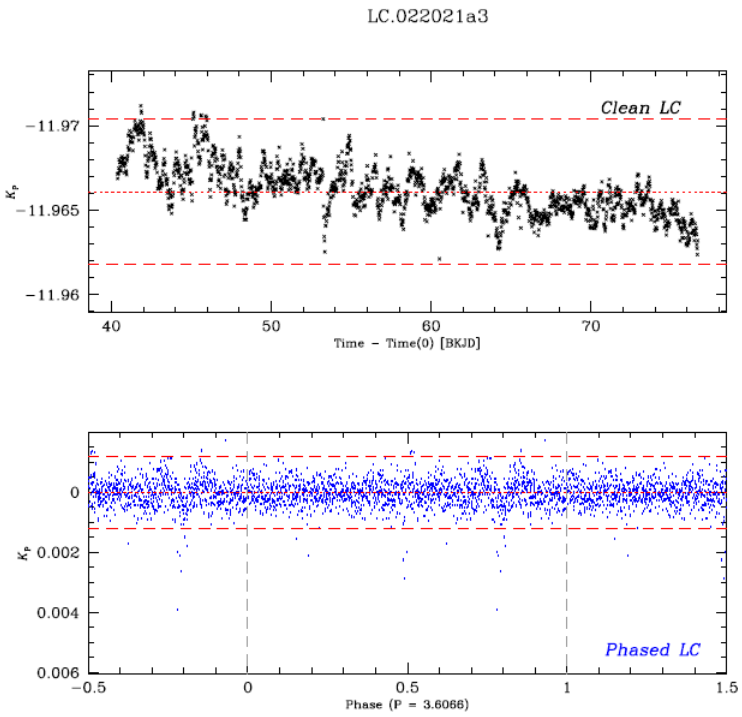

Figure 4.17: Same as in figure 4.15 but for star #22021.

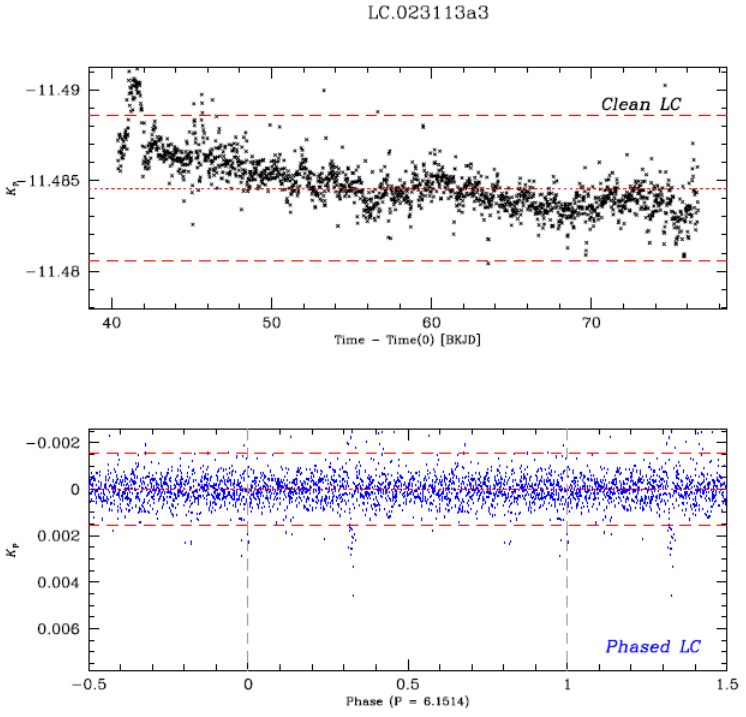

Figure 4.18: Same as in figure 4.15 but for star #23113.

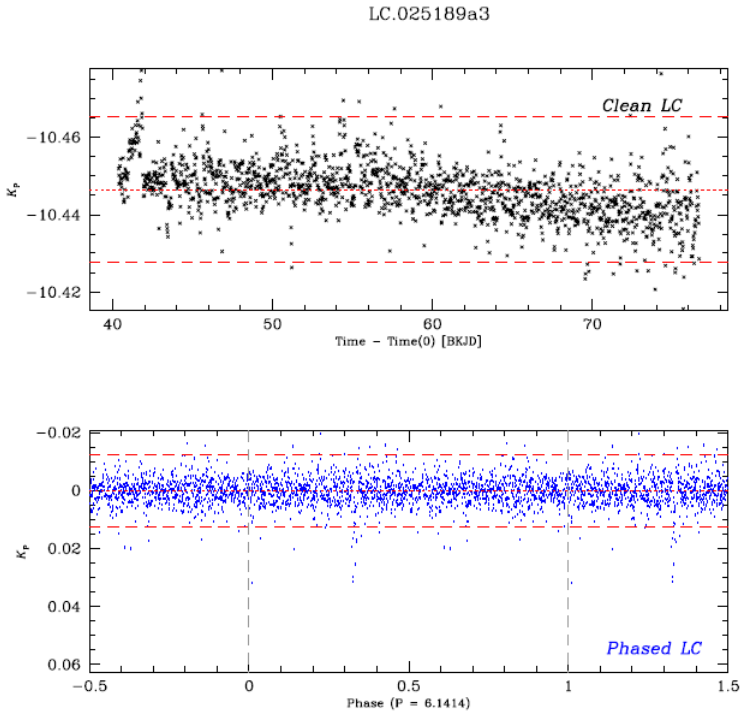

Figure 4.19: Same as in figure 4.15 but for star #25189.

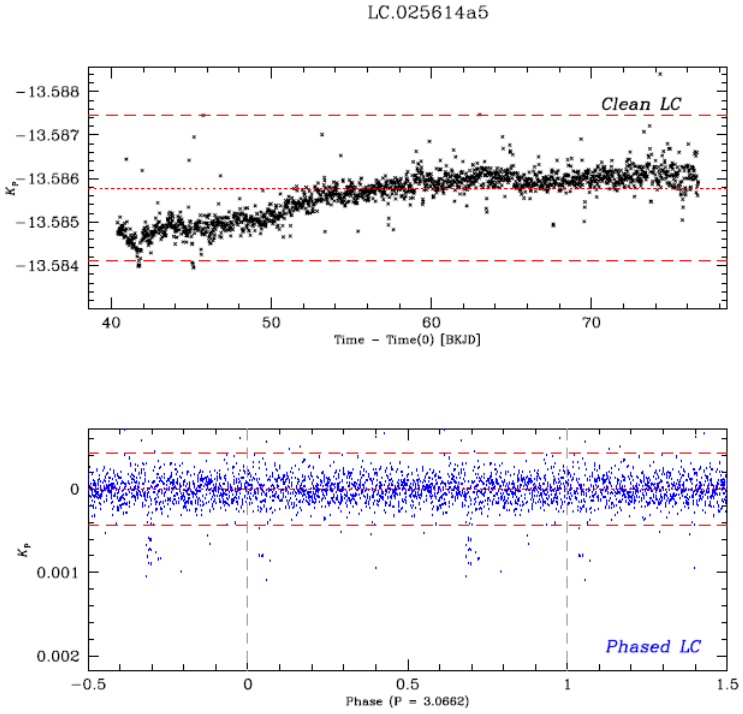

Figure 4.20: Same as in figure 4.15 but for star #25614.

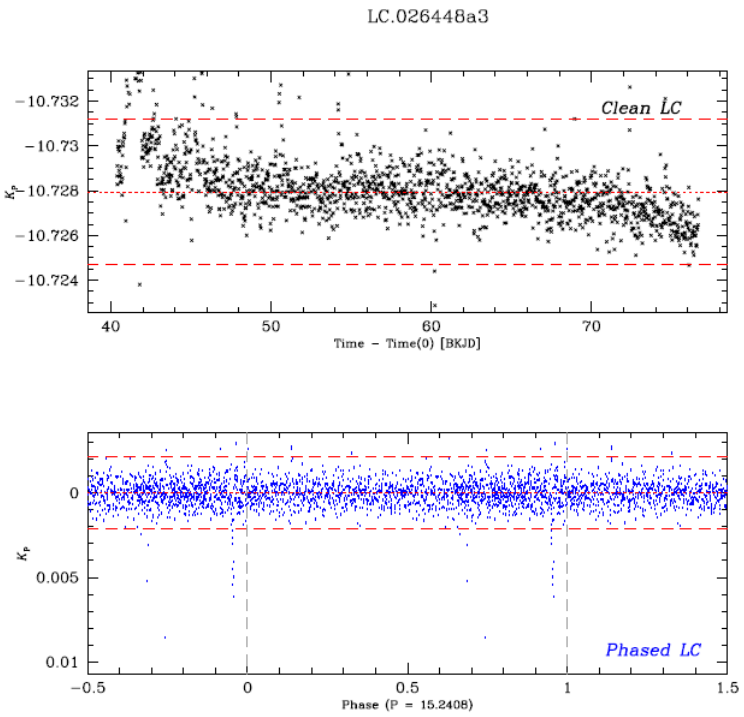

Figure 4.21: Same as in figure 4.15 but for star #26448.

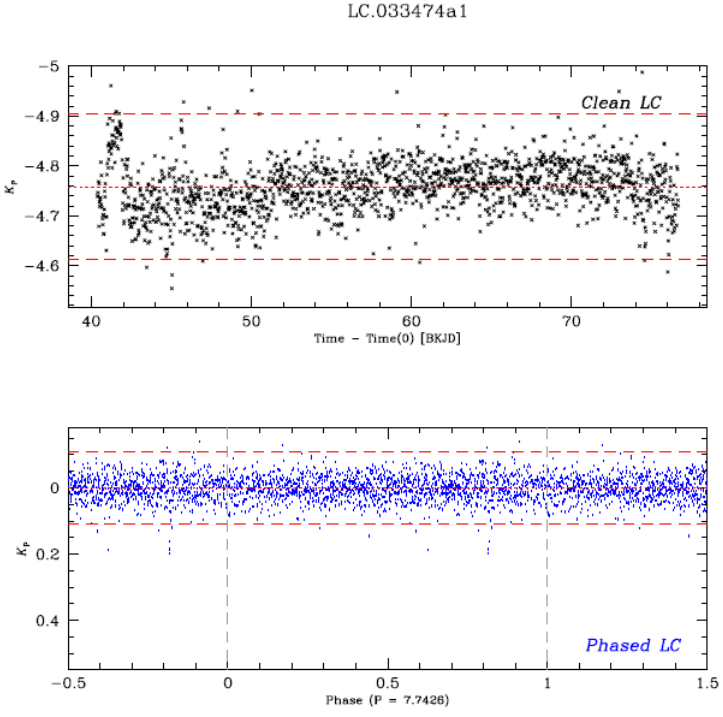

Figure 4.22: Same as in figure 4.15 but for star #33474.

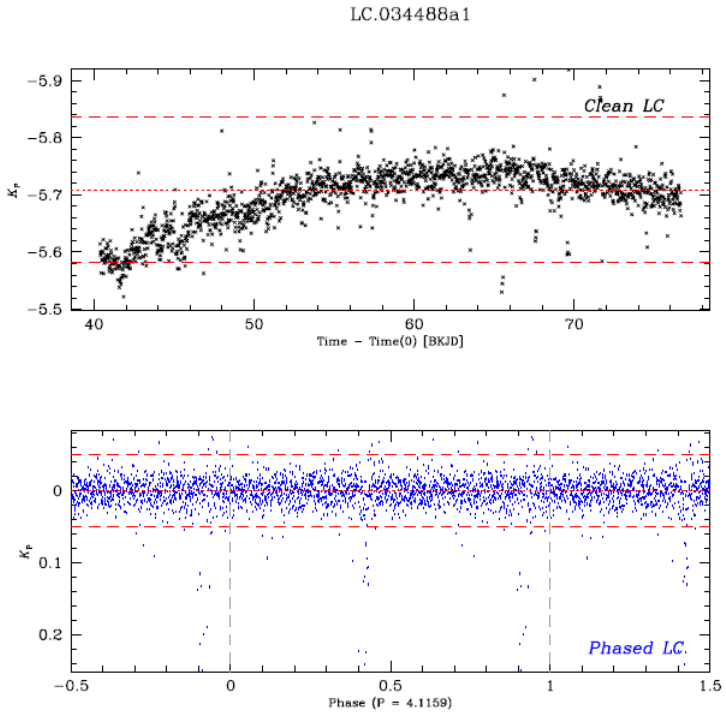

Figure 4.23: Same as in figure 4.15 but for star #34488.

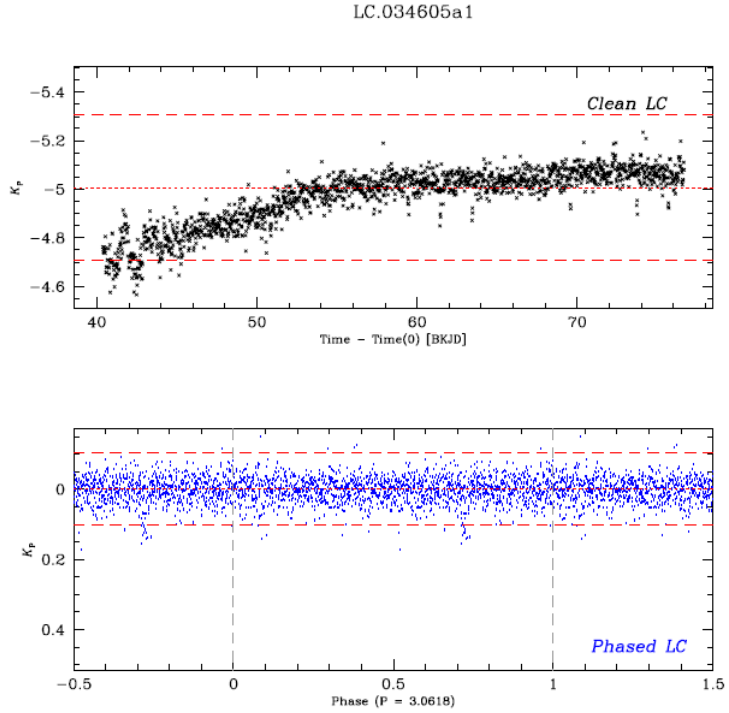

Figure 4.24: Same as in figure 4.15 but for star #34605.

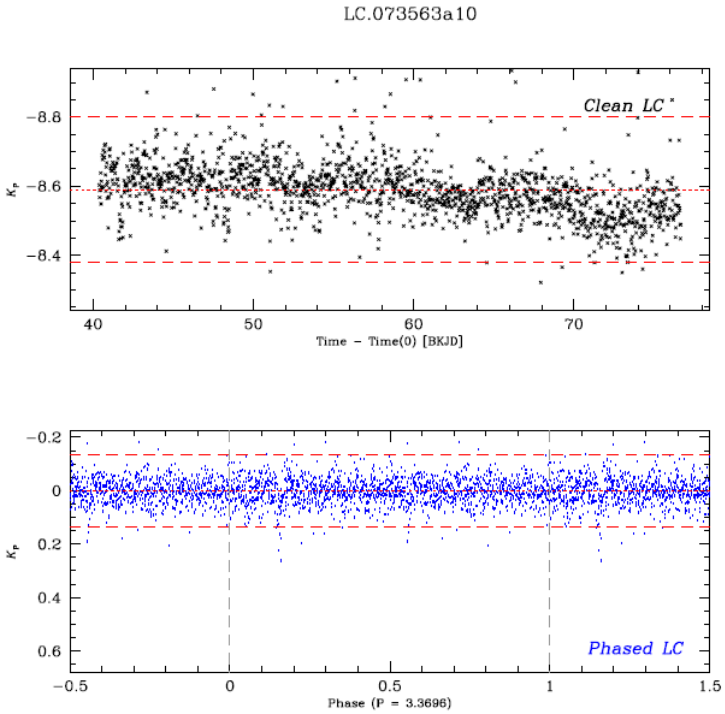

Figure 4.25: Same as in figure 4.15 but for star #73563.

4.6 First Candidate: Star #7139

From now on, I mark this light curve as a possible exoplanet candidate. In figure 4.26 it can be seen that the star could be a member of the NGC 2158 since it is within 0.1 deg from the cluster center. It is not part of the M 35 according to DANCe catalog (Bouy et al. 2015). In figure 4.26 I have used a green circle to enclose most of NGC 2158 members close to the cluster center, since I did not know the proper motions of these stars.

As it is clear, the star is very close to NGC 2158 center. Then I made color-magnitude diagrams (CMD) of this star with different filters using the catalog of Nardiello et al. (2015). As can be seen in figure 4.27 the red dots represent the star. In the right CMD I used red horizontal line for the location of the star due to lack of K_{2MASS} band magnitude.

Furthermore, in figure 4.28 I made CMDs using only the stars within 0.1 deg from NGC 2158 center. Red dots and horizontal line again represent the location of the star.

In figure 4.29 I analyzed its light curves with different apertures. Normally, if the flux drop is due to a close-by binary system, increasing aperture sizes could show deeper flux drops in the light curve because more light would fall inside the aperture. However, I did not observe this behavior. In figure 4.30 the PSF-based light curve is shown. The "V" shape flux drop can be observed clearly. This evidence, together with the location of the star in the CMD (very close to the NGC 2158 main sequence, on the red side), let me think that this star could be an eclipsing binary member of NGC 2158. Proper motions and additional follow-ups are required to better characterize this object.

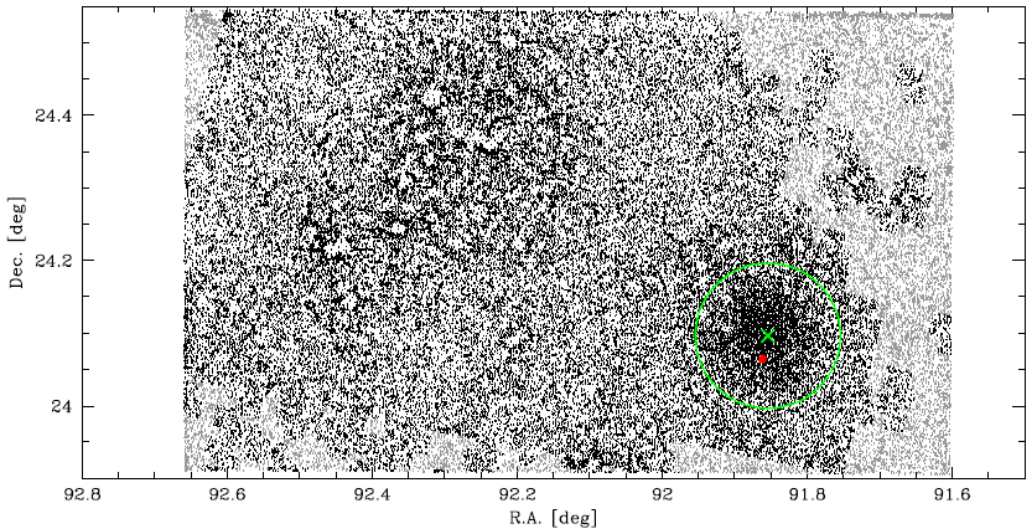

Figure 4.26: Position of all stars contained in the high-angular-resolution input catalog of Nardiello et al. (2015) used by Libralato et al. (2016a) for the light-curve extraction. The black points represent stars for which Libralato et al. (2016a) obtained a light curve from *K2*/C0 data, while the grey dots represents stars not imaged during this first *K2* campaign. The green cross represents the NGC 2158 cluster center and red dot shows the position of the star #7139. The green circle of 0.1-deg radius encloses most of NGC 2158 members.

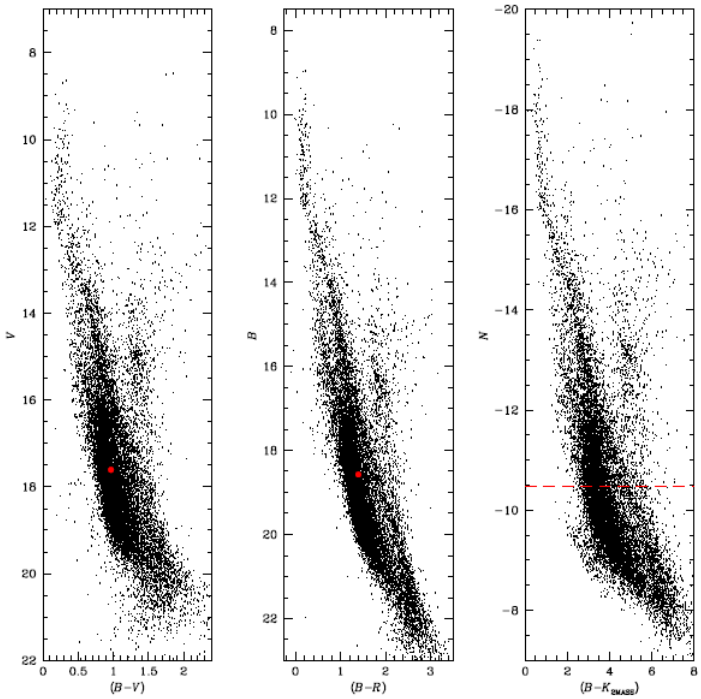

Figure 4.27: The color-magnitude diagrams obtained with the catalog from Nardiello et al. (2015) Red dots represent the position of the star #7139 in the CMDs. Since the $K_{\rm 2MASS}$ band magnitude of this star is not available, I drew a red horizontal line as reference.

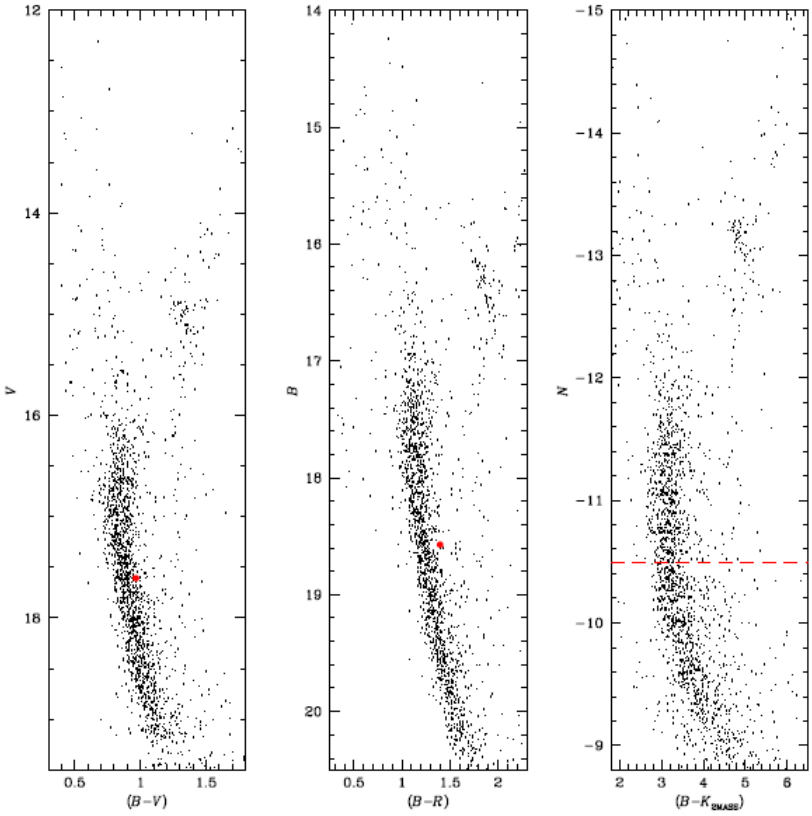

Figure 4.28: Same as in figure 4.30 but using only stars within 0,1 deg from NGC 2158 center.

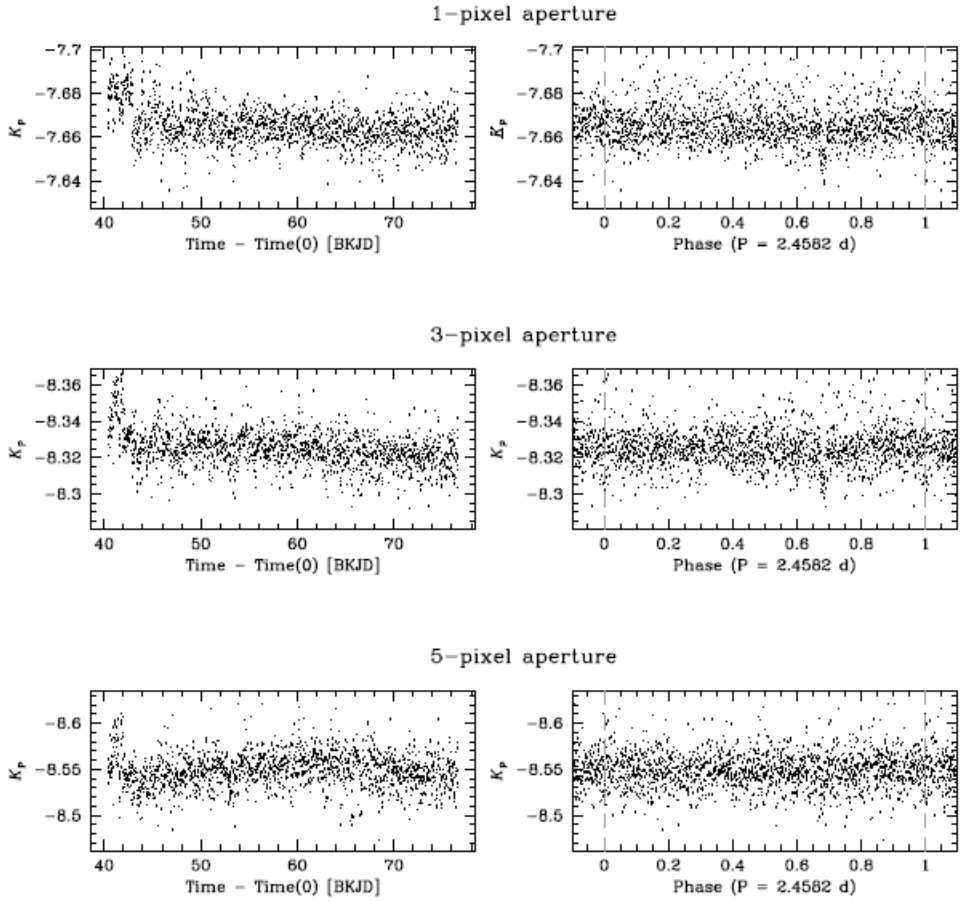

Figure 4.29: Clean and phased flat light curve of the star #7139 obtained with 1-pixel (top panel), 3-pixel (middle panel) and 5-pixel (bottom panel) aperture photometry.

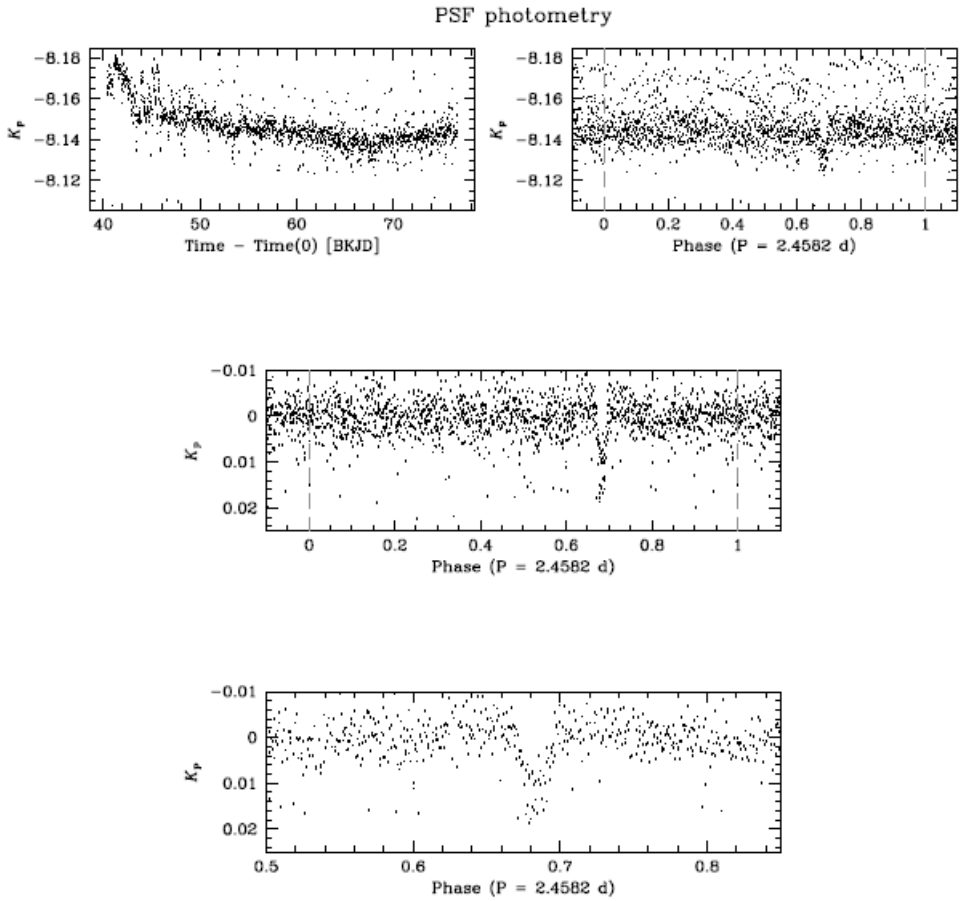

Figure 4.30: PSF-based light curve of this star #7139. In the middle and bottom panels, I zoomed-in around the flux drop and its "V" shape can be seen more clearly.

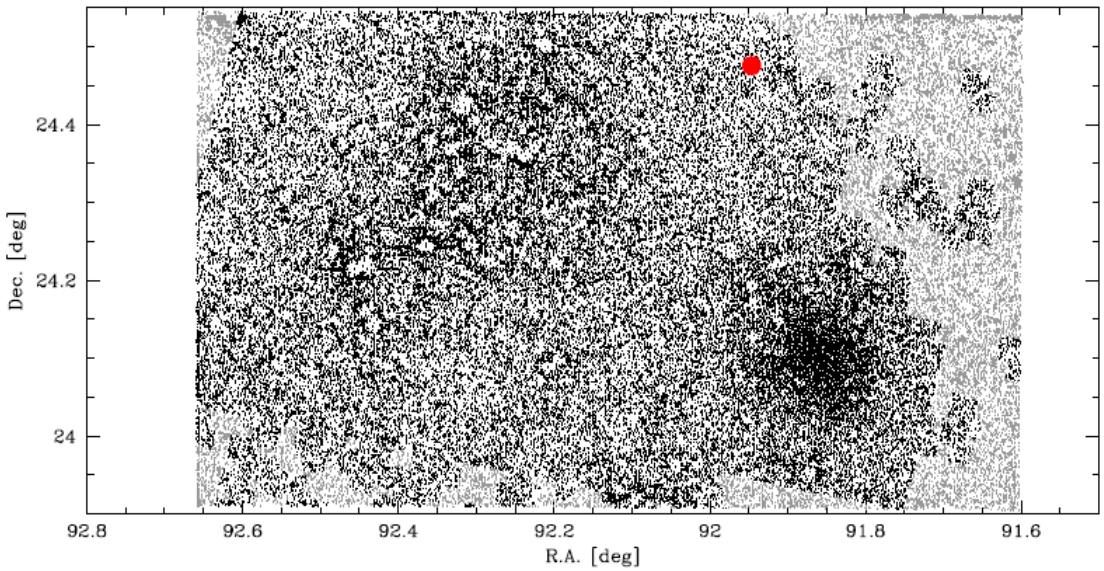

Figure 4.31: Same as figure 4.26. The red dot shows the position of the star #26448.

4.7 Second Candidate: Star #26448

The light curve LC.026448 was looking very promising. I checked the location of the star and it was not located near the NGC 2158 center. In figure 4.31 the location of the star can be seen as red dot. According to DANCe catalog proper motions, this star is not a member of M 35, therefore there is a high probability that is a field star.

Furthermore, when I checked the color-magnitude diagrams, I understood that probably it was not part of the NGC 2158 and M 35 and again it looks like it is a field star. The location of this star in different CMD can be seen in figure 4.32. Again these CMDs were created using the catalog of Nardiello et al. (2015).

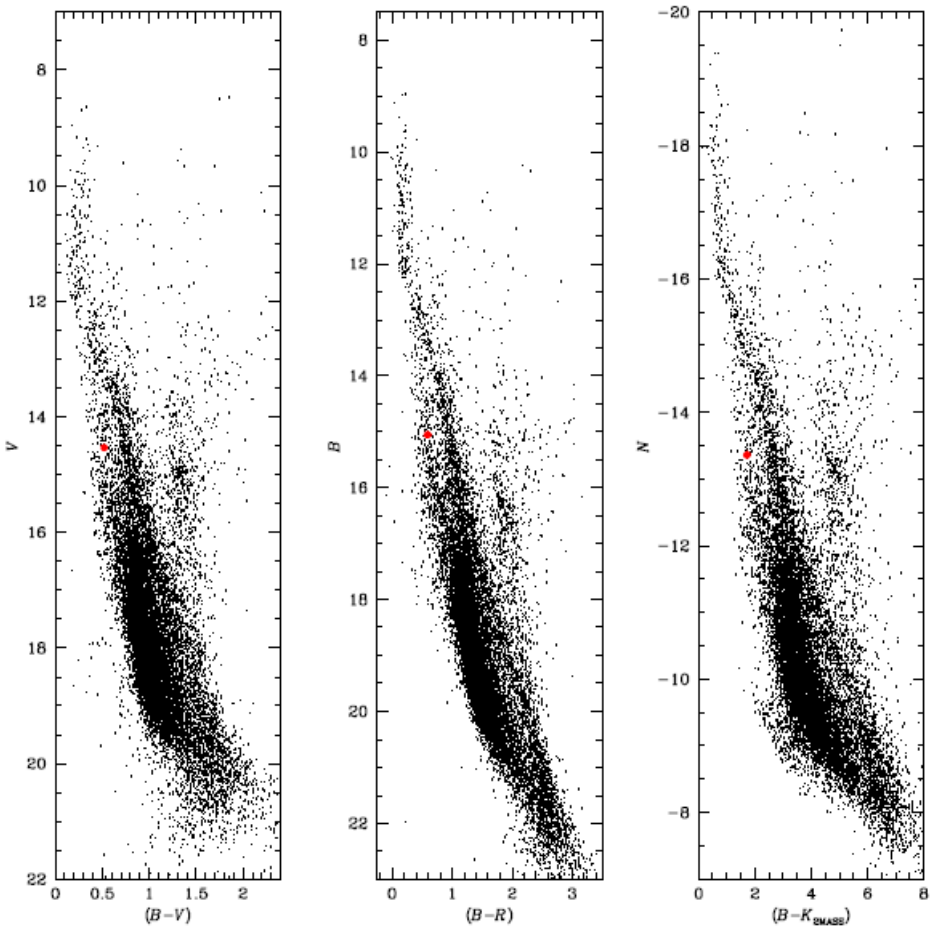

Figure 4.32: Same as figure 4.27, but for the star #26448.

In figure 4.33, I have compared the light curves obtained with different pixel apertures and found that the larger the aperture the deeper the flux drop. However, there is not any evident close-by eclipsing binary. Therefore for this object additional follow-ups and analysis are required. Another possibility of this flux drop could be uncorrected systematic effects.

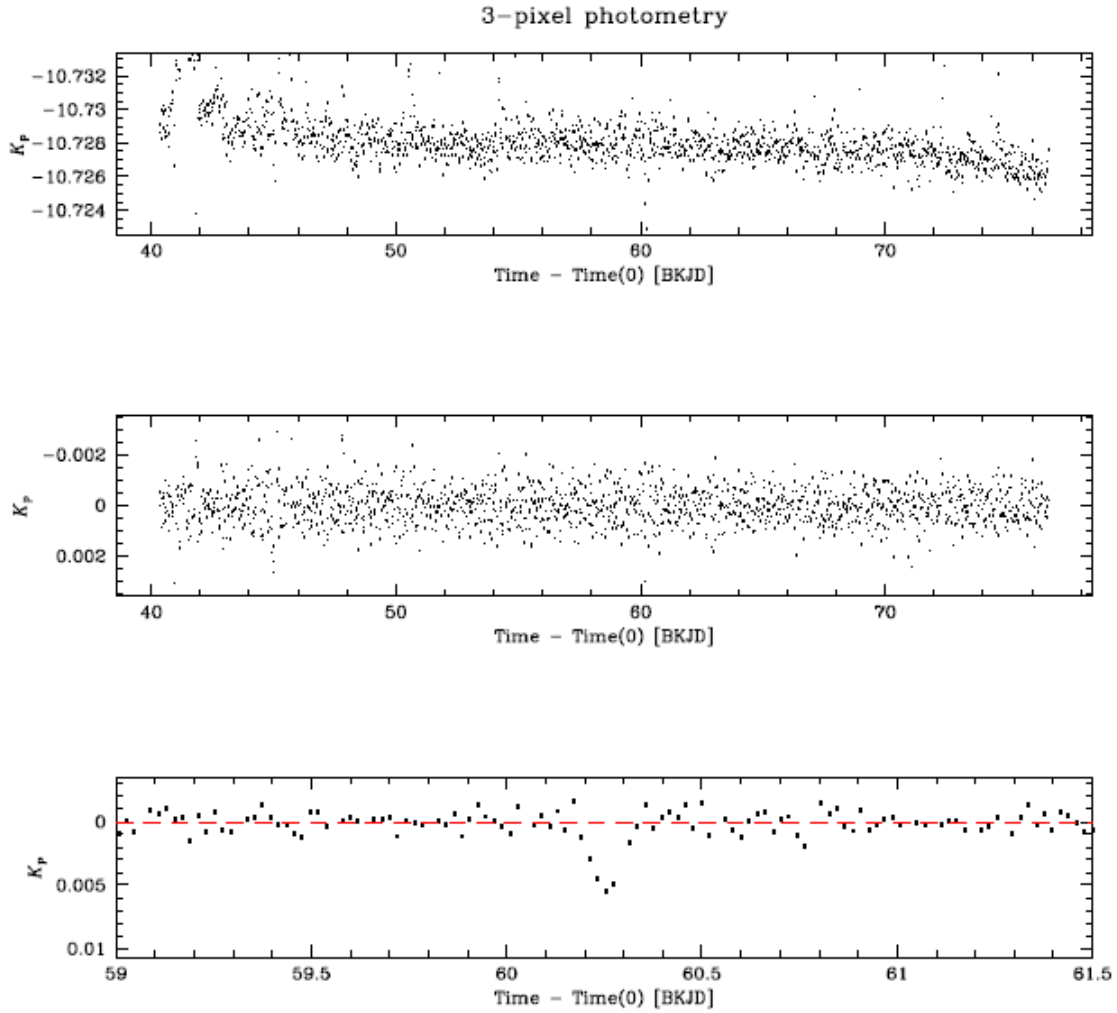

Figure 4.33: 3-pixels aperture-photometry light curve for this star #26448. In middle and bottom panels, I zoomed-in close to the flux drop.

Chapter 5

CONCLUSION AND FUTURE PROJECTS

In this project, I have worked on the *Kepler/K2* Campaign 0 data focusing on the open clusters M 35 and NGC 2158 to search for possible transiting exoplanet candidates. I used the light curves extracted by Libralato et al. (2016a). In their work, they used a high-angular-resolution input catalog and PSFs to subtract all close-by neighbors to a given target star before measuring its flux. This way they showed that they were able to decrease the light dilution effects and to obtain high-precision photometry for faint stars and in crowded environments.

First of all, I compared classical aperture photometry (with different aperture radii: 1 pixel, 3 pixels, 5 pixels, 10 pixels) with PSF photometry and understood that while 3-, 5-, 10-pixels aperture photometric methods perform better for bright stars, PSF and 1-pixel aperture photometric methods work best for faint stars (K_P >15.5) and in crowded environments.

Among all light curves obtained for the stars in the open clusters M 35 and NGC 2158, I found two (out of 54 922) light curves that show possible transit signals. One of them (star #26448) shows only one transit over the entire *K2*/C0. This flux drop could be due to an uncorrected systematic, blended eclipsing binary or a genuine transiting exoplanet with an orbital period greater than 35 days. I analyzed its light curves and its location in the CMDs and I was not able to rule out any of the previous conclusions. The second object (star #7139) is probably a NGC 2158 eclipsing binary accordingly to its location in the CMD and its "V"-shape flux drops. For these two objects more data is needed in order to understand their true nature.

The PSF-based approach developed by Nardiello et al. (2015) and Libralato et al. (2016a) can be used with every kind of data obtained either

from ground-based or space-based facilities. Future mission like TESS (Transiting Exoplanet Survey Satellite; Ricker et al. 2014) and PLATO (PLAnetary Transits and stellar Observation; Rauer et al. 2014) will observe different fields across the Galaxy to search for transiting exoplanets and this PSF-based light-curve extraction method will be very useful to analyze all crowded environments will be imaged.

Bibliography

S. Aigrain, J. Llama, T. Ceillier, M. L. d. Chagas, J. R. A. Davenport, R. A. García, K. L. Hay, A. F. Lanza, A. McQuillan, T. Mazeh, J. R. de Medeiros, M. B. Nielsen, and T. Reinhold. Testing the recovery of stellar rotation signals from Kepler light curves using a blind hare-and-hounds exercise. MNRAS, 450:3211–3226, July 2015. doi: 10.1093/mnras/stv853.

J. Anderson and I. R. King. Toward High-Precision Astrometry with WFPC2. I. Deriving an Accurate Point-Spread Function. Publications of the Astronomical Society of the Pacific, 112:1360–1382, October 2000. doi: 10.1086/316632.

J.-L. Beuzit, M. Feldt, K. Dohlen, D. Mouillet, P. Puget, F. Wildi, L. Abe, J. Antichi, A. Baruffolo, P. Baudoz, A. Boccaletti, M. Carbillet, J. Charton, R. Claudi, M. Downing, C. Fabron, P. Feautrier, E. Fedrigo, T. Fusco, J.-L. Gach, R. Gratton, T. Henning, N. Hubin, F. Joos, M. Kasper, M. Langlois, R. Lenzen, C. Moutou, A. Pavlov, C. Petit, J. Pragt, P. Rabou, F. Rigal, R. Roelfsema, G. Rousset, M. Saisse, H.-M. Schmid, E. Stadler, C. Thalmann, M. Turatto, S. Udry, F. Vakili, and R. Waters. SPHERE: a 'Planet Finder' instrument for the VLT. In Ground-based and Airborne Instrumentation for Astronomy II, volume 7014 of Proc. SPIE, page 701418, July 2008. doi: 10.1117/12.790120.

W. J. Borucki, D. G. Koch, J. J. Lissauer, G. S. Basri, D. A. Caldwell, E. DeVore, J. M. Jenkins, J. J. Caldwell, J. Christensen-Dalsgaard, W. D. Cochran, E. W. Dunham, T. N. Gautier, J. C. Geary, D. A. Latham, D. Sasselov, R. L. Gilliland, A. Gould, S. B. Howell, Y. Kondo, and D. G. Monet. Kepler Mission: Current Status. In American Astronomical Society Meeting Abstracts, volume 37 of Bulletin of the American Astronomical Society, page 1412, December 2005.

H. Bouy, E. Bertin, L. M. Sarro, D. Barrado, E. Moraux, J. Bouvier, J.-C. Cuillandre, A. Berihuete, J. Olivares, and Y. Beletsky. The Seven Sisters DANCe. I. Empirical isochrones, luminosity, and mass functions of the

Pleiades cluster. A&A, 577:A148, May 2015. doi: 10.1051/0004-6361/201425019.

D. Charbonneau, T. M. Brown, D. W. Latham, and M. Mayor. Detection of Planetary Transits Across a Sun-like Star. ApJ, 529:L45–L48, January 2000. doi: 10.1086/312457.

J. Christensen-Dalsgaard, H. Kjeldsen, T. M. Brown, R. L. Gilliland, T. Arentoft, S. Frandsen, P.-O. Quirion, W. J. Borucki, D. Koch, and J. M. Jenkins. Asteroseismic Investigation of Known Planet Hosts in the Kepler Field. ApJ, 713:L164–L168, April 2010. doi: 10.1088/2041-8205/713/2/L164.

D. A. Fischer, A. W. Howard, G. P. Laughlin, B. Macintosh, S. Mahadevan, J. Sahlmann, and J. C. Yee. Exoplanet Detection Techniques. Protostars and Planets VI, pages 715–737, 2014. doi: 10.2458/azu_uapress_9780816531240-ch031.

G. W. Henry, G. W. Marcy, R. P. Butler, and S. S. Vogt. A Transiting "51 Peg-like" Planet. ApJ, 529:L41–L44, January 2000. doi: 10.1086/312458.

S. B. Howell, C. Sobeck, M. Haas, M. Still, T. Barclay, F. Mullally, J. Troeltzsch, S. Aigrain, S. T. Bryson, D. Caldwell, W. J. Chaplin, W. D. Cochran, D. Huber, G. W. Marcy, A. Miglio, J. R. Najita, M. Smith, J. D. Twicken, and J. J. Fortney. The K2 Mission: Characterization and Early Results. Publications of the Astronomical Society of the Pacific, 126:398–408, April 2014. doi: 10.1086/676406.

P. Kalas, J. R. Graham, M. P. Fitzgerald, and M. Clampin. STIS Coronagraphic Imaging of Fomalhaut: Main Belt Structure and the Orbit of Fomalhaut b. ApJ, 775:56, September 2013. doi: 10.1088/0004-637X/775/1/56.

D. Koch, W. Borucki, G. Basri, T. Brown, D. Caldwell, J. Christensen-Dalsgaard, W. Cochran, E. Dunham, T. N. Gautier, J. Geary, R. Gilliland, J. Jenkins, Y. Kondo, D. Latham, J. Lissauer, and D. Monet. The Kepler Mission: Astrophysics and Eclipsing Binaries. Ap&SS, 304:391–395, August 2006. doi: 10.1007/s10509-006-9149-1.

D. G. Koch, W. Borucki, E. Dunham, J. Geary, R. Gilliland, J. Jenkins, D. Latham, E. Bachtell, D. Berry, W. Deininger, R. Duren, T. N. Gautier, L. Gillis, D. Mayer, C. D. Miller, D. Shafer, C. K. Sobeck, C. Stewart, and M. Weiss. Overview and status of the Kepler Mission. In J. C. Mather, editor, Optical, Infrared, and Millimeter Space Telescopes, volume 5487 of Proc. SPIE, pages 1491–1500, October 2004. doi: 10.1117/12.552346.

G. Kovács, S. Zucker, and T. Mazeh. A box-fitting algorithm in the search for periodic transits. A&A, 391:369–377, August 2002. doi: 10.1051/0004-6361:20020802.

M. Libralato, L. R. Bedin, D. Nardiello, and G. Piotto. A PSF-based approach to Kepler/K2 data - I. Variability within the K2 Campaign 0 star clusters M 35 and NGC 2158. MNRAS, 2016a.

M. Libralato, D. Nardiello, L. R. Bedin, L. Borsato, V. Granata, L. Malavolta, G. Piotto, P. Ochner, A. Cunial, and V. Nascimbeni. A PSF-based approach to Kepler/K2 data - II. Exoplanet candidates in Praesepe (M 44). MNRAS, 2016b.

M. N. Lund, R. Handberg, G. R. Davies, W. J. Chaplin, and C. D. Jones. K2P^2 A Photometry Pipeline for the K2 Mission. ApJ, 806:30, June 2015. doi: 10.1088/0004-637X/806/1/30.

C. Marois, B. Zuckerman, Q. M. Konopacky, B. Macintosh, and T. Barman. Images of a fourth planet orbiting HR 8799. Nature, 468:1080–1083, December 2010. doi: 10.1038/nature09684.

D. Nardiello, L. R. Bedin, V. Nascimbeni, M. Libralato, A. Cunial, G. Piotto, A. Bellini, L. Borsato, K. Brogaard, V. Granata, L. Malavolta, A. F. Marino, A. P. Milone, P. Ochner, S. Ortolani, L. Tomasella, M. Clemens, and M. Salaris. Variable stars in two open clusters within the Kepler/K2-Campaign-0 field: M35 and NGC 2158. MNRAS, 447:3536–3547, March 2015. doi: 10.1093/mnras/stu2697.

D. Nardiello, M. Libralato, L. R. Bedin, G. Piotto, L. Borsato, V. Granata, L. Malavolta, and V. Nascimbeni. A PSF-based approach toKepler/K2data - III. Search for exoplanets and variable stars within the open cluster M 67 (NGC 2682). MNRAS, 463:1831–1843, December 2016. doi: 10.1093/mnras/stw2169.

M. A. C. Perryman. Extra-solar planets. Reports on Progress in Physics, 63: 1209–1272, August 2000. doi: 10.1088/0034-4885/63/8/202.

H. Rauer, C. Catala, C. Aerts, T. Appourchaux, W. Benz, A. Brandeker, J. Christensen-Dalsgaard, M. Deleuil, L. Gizon, M.-J. Goupil, M. Güdel, E. Janot-Pacheco, M. Mas-Hesse, I. Pagano, G. Piotto, D. Pollacco, Ċ. Santos, A. Smith, J.-C. Suárez, R. Szabó, S. Udry, V. Adibekyan, Y. Alibert, J.-M. Almenara, P. Amaro-Seoane, M. A.-v. Eiff, M. Asplund, E. Antonello, S. Barnes, F. Baudin, K. Belkacem, M. Bergemann, G. Bihain, A. C. Birch, X. Bonfils, I. Boisse, A. S. Bonomo, F. Borsa, I. M.

Brandão, E. Brocato, S. Brun, M. Burleigh, R. Burston, J. Cabrera, S. Cassisi, W. Chaplin, S. Charpinet, C. Chiappini, R. P. Church, S. Csizmadia, M. Cunha, M. Damasso, M. B. Davies, H. J. Deeg, R. F. Díaz, S. Dreizler, C. Dreyer, P. Eggenberger, D. Ehrenreich, P. Eigmüller, A. Erikson, R. Farmer, S. Feltzing, F. de Oliveira Fialho, P. Figueira, T. Forveille, M. Fridlund, R. A. García, P. Giommi, G. Giuffrida, M. Godolt, J. Gomes da Silva, T. Granzer, J. L. Grenfell, A. Grotsch-Noels, E. Günther, C. A. Haswell, A. P. Hatzes, G. Hébrard, S. Hekker, R. Helled, K. Heng, J. M. Jenkins, A. Johansen, M. L. Khodachenko, K. G. Kislyakova, W. Kley, U. Kolb, N. Krivova, F. Kupka, H. Lammer, A. F. Lanza, Y. Lebreton, D. Magrin, P. Marcos-Arenal, P. M. Marrese, J. P. Marques, J. Martins, S. Mathis, S. Mathur, S. Messina, A. Miglio, J. Montalban, M. Montalto, M. J. P. F. G. Monteiro, H. Moradi, E. Moravveji, C. Mordasini, T. Morel, A. Mortier, V. Nascimbeni, R. P. Nelson, M. B. Nielsen, L. Noack, A. J. Norton, A. Ofir, M. Oshagh, R.-M. Ouazzani, P. Pápics, V. C. Parro, P. Petit, B. Plez, E. Poretti, A. Quirrenbach, R. Ragazzoni, G. Raimondo, M. Rainer, D. R. Reese, R. Redmer, S. Reffert, B. Rojas-Ayala, I. W. Roxburgh, S. Salmon, A. Santerne, J. Schneider, J. Schou, S. Schuh, H. Schunker, A. Silva-Valio, R. Silvotti, I. Skillen, I. Snellen, F. Sohl, S. G. Sousa, A. Sozzetti, D. Stello, K. G. Strassmeier, M. Švanda, G. M. Szabó, A. Tkachenko, D. Valencia, V. Van Grootel, S. D. Vauclair, P. Ventura, F. W. Wagner, N. A. Walton, J. Weingrill, S. C. Werner, P. J. Wheatley, and K. Zwintz. The PLATO 2.0 mission. Experimental Astronomy, 38: 249–330, November 2014. doi: 10.1007/s10686-014-9383-4.

J. Renn, T. Sauer, and J. Stachel. The origin of gravitational lensing: a postscript to Einstein's 1936 Science paper. Science, 275:184–186, January 1997. doi: 10.1126/science.275.5297.184.

G. R. Ricker, J. N. Winn, R. Vanderspek, D. W. Latham, G. Á. Bakos, J. L. Bean, Z. K. Berta-Thompson, T. M. Brown, L. Buchhave, N. R. Butler, R. P. Butler, W. J. Chaplin, D. Charbonneau, J. Christensen-Dalsgaard, M. Clampin, D. Deming, J. Doty, N. De Lee, C. Dressing, E. W. Dunham, M. Endl, F. Fressin, J. Ge, T. Henning, M. J. Holman, A. W. Howard, S. Ida, J. Jenkins, G. Jernigan, J. A. Johnson, L. Kaltenegger, N. Kawai, H. Kjeldsen, G. Laughlin, A. M. Levine, D. Lin, J. J. Lissauer, P. MacQueen, G. Marcy, P. R. McCullough, T. D. Morton, N. Narita, M. Paegert, E. Palle, F. Pepe, J. Pepper, A. Quirrenbach, S. A. Rinehart, D. Sasselov, B. Sato, S. Seager, A. Sozzetti, K. G. Stassun, P. Sullivan, A. Szentgyorgyi, G. Torres, S. Udry, and J. Villasenor. Transiting Exoplanet Survey Satellite (TESS). In Space Telescopes and Instrumentation 2014: Optical,

Infrared, and Millimeter Wave, volume 9143 of Proc. SPIE, page 914320, August 2014. doi: 10.1117/12.2063489.

J. Sahlmann, P. F. Lazorenko, D. Ségransan, E. L. Martín, D. Queloz, M. Mayor, and S. Udry. Astrometric orbit of a low-mass companion to an ultracool dwarf. A&A, 556:A133, August 2013. doi: 10.1051/0004-6361/201321871.

P. Schneider. Gravitational lenses. 1999.

A. Vanderburg and J. A. Johnson. A Technique for Extracting Highly Precise Photometry for the Two-Wheeled Kepler Mission. Publications of the Astronomical Society of the Pacific, 126:948–958, October 2014. doi: 10.1086/678764.

A. Vanderburg, D. W. Latham, L. A. Buchhave, A. Bieryla, P. Berlind, M. L. Calkins, G. A. Esquerdo, S. Welsh, and J. A. Johnson. Planetary Candidates from the First Year of the K2 Mission. ApJS, 222:14, January 2016. doi: 10.3847/0067-0049/222/1/14.